Article

Palaeoclimatic Inferences from Clayey-Iron Palaeosols: A Weathering Event Recorded in the Middle–Upper Jurassic Unconformity (South Iberian Palaeomargin, Western Tethys)

Elisa Laita * , Isabel Abad and Matías Reolid

Departamento de Geología & Centro de Estudios Avanzados en Ciencias de la Tierra, Energía y Medio Ambiente (CEACTEMA), Universidad de Jaén, Campus Las Lagunillas sn, 23071 Jaén, Spain; miabad@ujaen.es (I.A.); mreolid@ujaen.es (M.R.)
* Correspondence: elaita@ujaen.es

Abstract: The study of iron crusts containing iron-coated grains from different sections of the Prebetic (SE Iberia) and the overlying marine sedimentary rocks also containing iron-coated grains in the Prebetic and the Iberian Range (NE Iberia) allowed us to determine the palaeoclimatic and palaeoenvironmental conditions under which they originated. The iron crusts are mainly composed of clay minerals (kaolinite and illitic phases) and/or goethite and hematite. The kaolinite texture indicates that it is authigenic, whereas the illitic phases are probably detrital. The mineralogy and texture of the iron crusts allow us to classify them as plinthitic palaeosols. The iron-coated grains consisting of a nucleus and a cortex, both composed of a mixture of kaolinite, goethite, and hematite, originated in situ during the plinthite development. Reworking processes caused the fragmentation and incorporation of the iron-coated grains into the overlying ferruginous oolithic limestones and terrigenous-carbonated breccia. New marine iron-coated grains formed later in the ferruginous oolithic limestones. The high Chemical Index of Alteration and Chemical Index of Weathering values and the geochemical ratios (Ba/Sr, Rb/Sr, Sr/Cu, Ga/Rb) from iron deposits reflect intense weathering under warm and humid conditions in the South Iberian Palaeomargin during the Callovian–Oxfordian, which may also take place in the East Iberian Palaeomargin (Iberian Range).

Keywords: geochemical ratios; illitic phases; iron-coated grains; iron crusts; kaolinite; palaeoclimate; plinthite

1. Introduction

Clay minerals can be found in soils, sediments, and numerous sedimentary rocks at the Earth's surface. The genesis of clay minerals occurs predominantly in areas where chemical weathering and edaphic processes (i.e., related to soil) take place, which are strongly controlled by climatic factors such as temperature and precipitation [1,2]. Consequently, the study of clay minerals from palaeosols (i.e., soils developed in the landscapes of the past) gives key information for palaeoclimatic and palaeoenvironmental reconstructions [3–6].

Variations in clay mineral assemblages formed in palaeosols developed in Mesozoic successions have been used as palaeoclimatic and palaeoenvironmental proxies [6–9].

Intense chemical weathering processes occur under warm and humid conditions (subtropical to tropical), giving place to a very effective hydrolysis resulting in the genesis of oxisols (according to the USDA (United States Department of Agriculture) soil taxonomy) and bauxites. In these tropical soils, kaolinite is the main clay mineral together with Al hydroxides and Fe oxyhydroxides [1–3,6,9–11].

Palaeosols can contain not only authigenic clay minerals formed by chemical weathering but also clay minerals of different origins (detrital or diagenetic). This must be taken into account when using clay minerals as palaeoclimatic and palaeoenvironmental proxies. Detrital minerals are inherited and will, therefore, reflect the weathering processes

developed in the source area, whereas diagenetic processes can modify the association of clay minerals (both detrital and authigenic), transforming them into new diagenetic phases and then invalidating the use of authigenic clay minerals as palaeoclimatic and palaeoenvironmental proxies [6,8,9,12–14].

The worldwide loss of carbonate productivity from the Late Callovian to Early Oxfordian has been attributed to climatic and oceanographic changes [15,16]. Oxygen isotope data point to a progressive cooling of the ocean waters from Middle Callovian to Early Oxfordian with the subsequent sea-level fall and the erosion of carbonate platforms resulting in common unconformities in wide areas, for example, in the Tethys [17–21]. Subsequently, a warming event occurred during the Middle Oxfordian [15,22–25]. The $\delta^{18}O$ variations also reflect precipitation regimes against a general warm climate for the Middle to Late Oxfordian [15,16].

During the Middle–Late Jurassic transition, the Tethyan Domain experienced important sea-level fluctuations due to the fragmentation of continental palaeomargins under an extensive rifting phase [21,26–28]. The fragmentation of continental palaeomargins and the sea level changes in the Western Tethys gave place to a stratigraphic unconformity recorded in different basins of western Europe and northern Africa [17–20,29–31].

Numerous regional studies describe the presence of this discontinuity in the External Prebetic of the Betic Cordillera (SE Iberia), which represents the Mesozoic sedimentation of the South Iberian Palaeomargin, with an iron crust containing iron-coated grains overlayed by ferruginous oolithic limestones [31]. This discontinuity has previously been characterized from a sedimentological, mineralogical, and geochemical point of view [21,32]. However, detailed characterization of the texture of the clay minerals assemblages in the iron crusts and the iron-coated grains is still lacking.

In this work, X-ray diffraction, optical and electron microscopy, and geochemical analysis have been carried out to undertake mineralogical characterization of the iron crust containing iron-coated grains to the Middle–Late Jurassic discontinuity of the External Prebetic, that represents proximal areas of the South Iberian Palaeomargin. New outcrops and those previously reported in the literature for the External Prebetic, are analyzed, including examples from the same discontinuity from the East Iberian Palaeomargin, represented by the Iberian Range. The analyses allow us: (1) to determine the origin of the clay minerals (authigenic, detrital, or diagenetic), (2) to evaluate the palaeoclimatic and palaeoenvironmental conditions under which these iron crust and iron-coated grains were generated during the Middle–Upper Jurassic transition in this area of the Betic Cordillera (SE Iberia), and (3) to compare the palaeoenvironmental conditions and processes occurring in the South Iberian Palaeomargin (External Prebetic) and the East Iberian Palaeomargin (Iberian Range).

2. Geological Setting

The Betic Cordillera, situated to the S and SE of the Iberian Peninsula, represents the western most sector of the European Alpine Orogen. Two main geological domains are differentiated in the Betic Cordillera: the Betic External Zones and the Betic Internal Zones [33]. The Betic External Zones comprise Mesozoic to Lower Neogene sedimentary rocks that were deposited in the South Iberian Palaeomargin (Western Tethys). The higher rank division of the Betic External Zones is into Prebetic and Subbetic [33,34]. Within the Jurassic paleogeography of the South Iberian Palaeomargin, the Prebetic represents a comparatively proximal epicontinental shelf, whereas the Subbetic represents distal epioceanic swell and through areas. According to stratigraphic and tectonic data, the Prebetic domain is subdivided into External and Internal Prebetic [33,35] (Figure 1). The Prebetic successions are mainly formed by shallow marine facies, with continental episodes and intervals of erosion, whereas pelagic facies are dominant in the Subbetic domain [33,36].
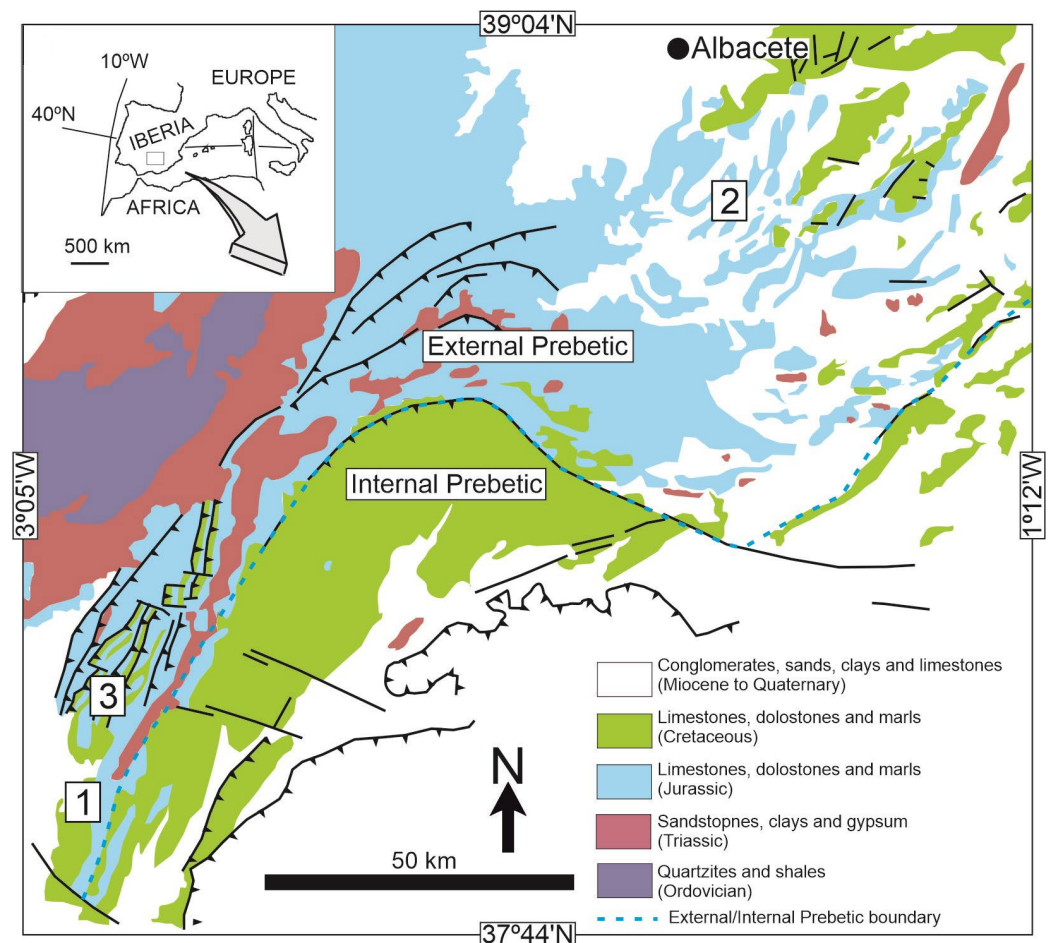
Figure 1. Geological map of the Betic Cordillera showing the Prebetic and its location on the Iberian Peninsula (SE Spain). The location of the previously studied outcrops by Reolid and Abad [21] and Reolid et al. [32] in the Central External Prebetic (1: RGCH, RGCHP, and CHO sections) and Eastern External Prebetic (2: PC1 to P4 sections) are represented together with the new outcrop analyzed in this study located in the north area of the Central External Prebetic (3: VI section). Modified from Reolid et al. [32].

The Middle–Upper Jurassic materials studied here are located in External Prebetic outcrops (Figures 1 and 2). During the Early–Middle Jurassic, the External Prebetic constituted a carbonate inner-self environment, which became a carbonate–siliciclastic mid-shelf environment during the Late Jurassic (Middle Oxfordian to Early–Middle Kimmeridgian) [37]. There is a discontinuity associated with the Middle/Upper Jurassic boundary [36,38].

In the Central External Prebetic, the Callovian/Oxfordian boundary is located between the carbonate deposits (Lower–Middle Jurassic) of the Chorro Formation [39,40] and the marl–limestone rhythmites (Middle–Upper Oxfordian) of the Lorente Formation [40,41]. The Chorro Formation encompasses approximately 400 m of Lower Jurassic dolomitized limestones, along with 50 m of Middle Jurassic oolithic limestones with megaripples and oncolithic–bioclastic facies [32]. The presence of *Protopeneroplis striata* [35,42], *Mesoendothyra croatica*, and *Trocholina palestiniensis* [38] confirms Middle Jurassic age and a shallow inner-shelf setting. The Upper Jurassic (Middle Oxfordian–Lower Kimmeridgian) Lorente Formation constitutes the onset of hemipelagic sedimentation within the southeastern epicontinental system. In the proximal sectors of the shelf, the Lorente Formation mainly consists of 70–100 m thick succession of marl–limestone rhythmites, as documented by Reolid [40] and Rodríguez-Tovar [43]. The Lorente Formation is commonly preceded by <1 m of spongiolithic limestones [44,45].
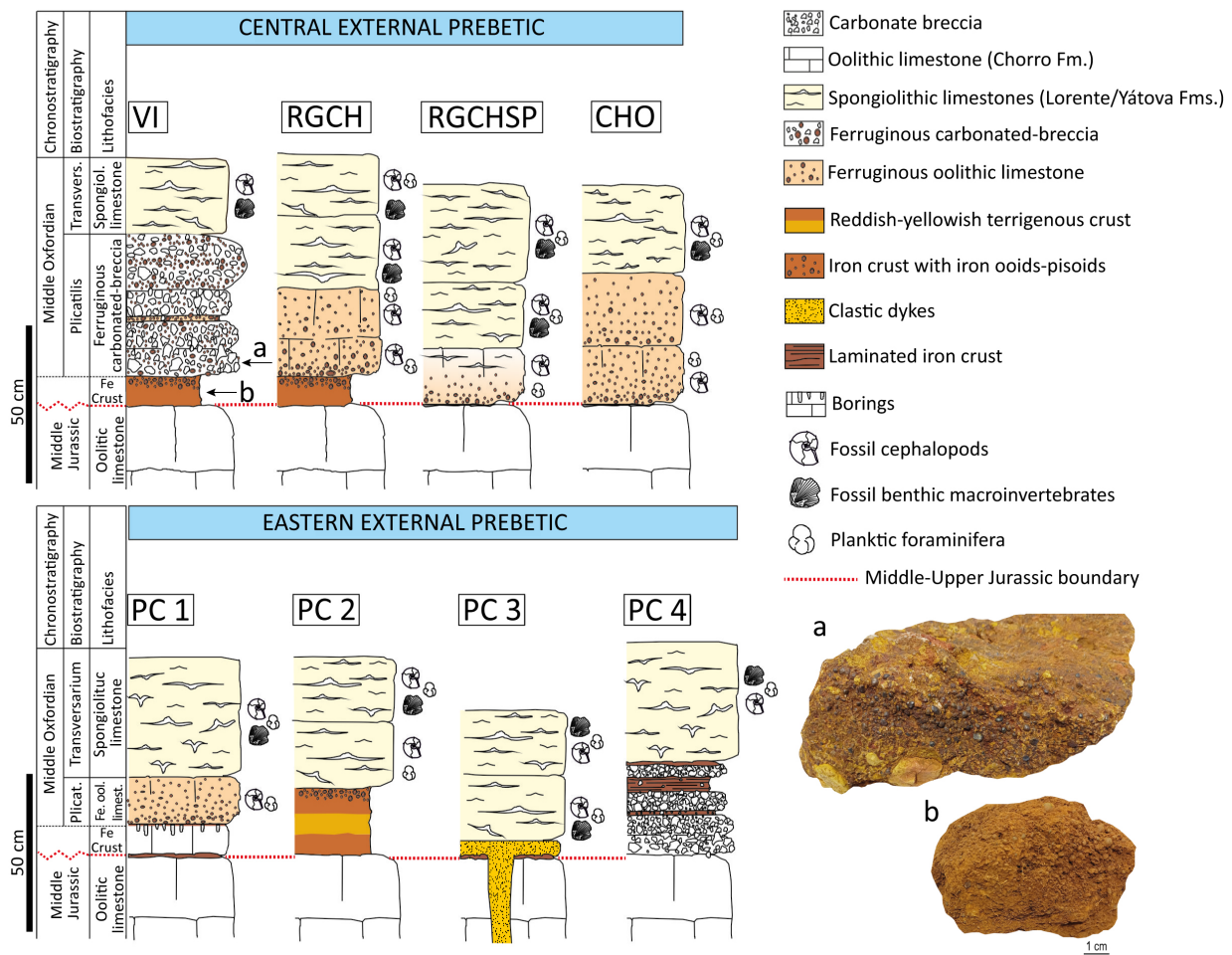
Figure 2. Sections from the central and eastern sectors of the External Prebetic showing the iron crusts and the ferruginous oolithic limestones in the Callovian–Oxfordian discontinuity (modified from Reolid and Abad [21]) and images of the ferruginous–carbonated breccia containing iron-coated grains (**a**) and the iron crust containing iron-coated grains (**b**) from the Villas (VI) section.

In the eastern sector, this discontinuity is located between the Chorro Formation and the spongiolithic limestones (Middle–Upper Oxfordian) of the Yátova Formation [46]. The spongiolithic limestones can reach around 16 m thick [44,45]. This stratigraphic succession of the Eastern External Prebetic is similar to that described in the Iberian Range [19,46].

Iron crusts containing iron-coated grains have been documented in relation to this Middle/Upper Jurassic discontinuity in the Sierra de Cazorla (Central External Prebetic) and Altos de Chinchilla (Eastern External Prebetic) [21,32] (Figure 2). These crusts are also observed in the Sierra de las Villas (north area of the Central External Prebetic), showing a palaeosols appearance (Figure 2). According to Reolid et al. [32], the discontinuity in the External Prebetic appears as a slightly irregular erosive surface with abundant iron oxides, which coincides with the palaeokarst previously described in the Eastern External Prebetic [21,47].

Ferruginous oolithic limestones (10–40 cm thick) occur over the iron crust in the central (Sierra de Cazorla) and eastern (Altos de Chinchilla) sectors of the External Prebetic [21,32] (Figure 2). Locally, these ferruginous oolithic limestones overlie the discontinuity surface directly and pinch out laterally [21,31,32,40]. This lithofacies correlates with the Arroyofrío Formation of the Iberian Range that preceded the spongiolithic limestone lithofacies of the Yátova Formation (SE Iberia) [19,46].

3. Samples and Methods

This work analyzes iron crusts and iron-coated grains from the External Prebetic sections previously studied by Reolid and Abad [21] and Reolid et al. [32]. Additionally, it includes a new outcrop located in the north area of the Central Prebetic (Sierra de las Villas, province of Jaén, SE Spain) (Figures 1 and 2). This new outcrop provides new sedimentary features, complementing the knowledge about the environmental conditions that occurred during the Middle–Upper Jurassic transition. In addition, this study includes samples from the equivalent ferruginous oolithic limestones from the neighbor domain, the Iberian Range, represented by the Arroyofrío Formation. With respect to previous works, this study is focused on the presence and palaeoenvironmental significance of clay minerals in these deposits.

Therefore, the studied outcrops are distributed in the Central External Prebetic, Eastern External Prebetic, and Iberian Range. The sections from the Central External Prebetic are located in the western nappes of the Sierra de Cazorla (province of Jaén, SE Spain): Riogazas-Chorro (RGCH, 37°52′22″ N, 3°0′26″ W), Riogazas-Chorro-SP (RGCHSP, 37°52′22″ N, 3°0′22″ W), and El Chorro (CHO, from 37°52′27″ N, 3°0′22″ W to 37°52′22″ N, 3°0′16″ W). The new outcrop in Sierra de las Villas (province of Jaén, SE Spain) is located 12 km north of the outcrops of Sierra de Cazorla: Villas (VI, 37°59′08″ N, 2°55′52″ W).

The sections from the Eastern External Prebetic are located in the Sierra del Chortal (province of Albacete, SE Spain): Pozo Cañada 1 (PC1, 38°47′36″ N, 1°43′25″ W), Pozo Cañada 2 (PC2, 38°47′37″ N, 1°43′25″ W), Pozo Cañada 3 (PC3, 38°47′45″ N, 1°43′18″ W) and Pozo Cañada 4 (PC4, 38°47′48″ N, 1°43′13″ W). This area is around 140 km northeast of the outcrops of the Central External Prebetic.

Finally, the iron-coated grains studied in the Iberian Range for comparing with the External Prebetic come from the Arroyofrío Formation of the Sierra de Albarracín (province of Teruel, E Spain): Gea de Albarracín (AF section, 40°24′45″ N, 1°19′56″ W). This outcrop is around 310 km northeast of the outcrops of the Central External Prebetic.

3.1. X-ray Diffraction Study

The matrix of the iron crust from Sierra de las Villas and the iron-coated grains separated from this matrix were analyzed by X-ray diffraction (XRD) from unoriented powders (whole rock analysis) to determine their mineralogical composition. The <2 μm fraction of the crust was extracted by centrifugation and was air-dried, and ethylene glycol-treated oriented aggregates were prepared by sedimentation on glass slides to determine the clay minerals present in the samples. To obtain the diffraction patterns, a PANalytical Empyrean diffractometer was used at the Scientific-Technical Instrumentation Center (CICT) of the University of Jaén (Spain), equipped with an X'Celerator solid-state linear detector and θ/θ goniometer, using CuKα radiation, 45 kV voltage and 40 mA current. The XRD patterns were acquired from 4° to 64° 2θ for the whole rock samples and from 4° to 32° 2θ for the <2 μm fraction. In both cases, a step increment of 0.01° 2θ and a counting time of 10s/step was used. The recording was made with XPowderX software (Version 2023.06.01) [48].

Relative proportions of the mineral phases were calculated using Reference Intensity Ratios (RIR) from the literature [49–51]. The RIR values were calculated following the procedure described by Hillier [52]. The Al^{3+} content in the goethite structure was calculated in the unoriented powder XRD patterns of the crust and the iron pisoids as an indicator of the origin of goethite [32,53], following the procedure proposed by Schulze [54] based on the position of de d_{110} and d_{111} peaks of goethite in the XRD patterns.

3.2. Optical and Electron Microscopy Study

Polished thin sections of the iron crust and the ferruginous–carbonated breccia from the Villas section were studied by optical microscopy to identify the minerals and characterize their texture. Polished thin sections of the ferruginous oolithic limestone from RGCH, CHO, and PC1 sections and the equivalent lithofacies of the AF section in the Iberian Range were

also studied by optical microscopy to characterize the texture of iron-coated grains and compare them with those from the Villas section. The iron-coated grains in the crust, the ferruginous oolithic limestone, and the ferruginous–carbonated breccia, are described as follows: macropisoids (>5 mm), pisoids (5–1 mm), ooids (1000–100 μm) and micro-ooids (<100 μm) [55].

The polished thin sections of the Villas section (the crust and the ferruginous–carbonated breccia) and rock fragments of the iron crust and the iron-coated grains were examined by Scanning Electron Microscopy (SEM) at the CICT (University of Jaén, Spain) using a Merlin Carl Zeiss Gemni II SEM. The polished thin sections and the rock fragments were previously carbon-coated. Compositional images were obtained using two detectors: an angular selective backscattered electron detector (AsB) and an energy selective backscattered electron detector (EsB). Chemical information and mapping were also obtained using an energy-dispersive X-ray spectroscopy (EDS). The accelerating voltage for the AsB and the EDS was 15 kV with a beam current of 750 pA, whereas for the EsB, the accelerating voltage was 4 kV with a beam current of 750 pA. For the rock fragments, morphological images were obtained using a secondary (In-lens) detector. In this case, the accelerating voltage was 5 kV with a beam current of 750 pA. A polished thin section of the ferruginous oolithic limestone from the AF section and rock fragments of the iron crust from the PC2 section were also studied by SEM using the same analytical conditions as for the Villas section samples. The purpose of studying these samples was to compare the mineralogy and texture of the clay minerals in the iron-coated grains of the AF section and the iron crust of the PC2 section with those observed in the Villas section.

For those figures containing XRD patterns, optical and SEM images, mineral abbreviations are according to Whitney and Evans [56].

3.3. Geochemical Study

Elemental mappings of the ferruginous–carbonated breccia from the Villas section have been obtained by an X-ray-microfluorescence M4 Tornado Brucker at the CICT (University of Jaén, Spain). The major elements of the matrix of the iron crust and the iron-coated grains from the Villas section were analyzed separately using X-ray fluorescence (XRF) in a PANalytical Zetium spectrometer with a maximum power of 4 kW and provided with an X-ray tube of Rh anode. Trace element analyses were carried out using a PerkinElmer NexION 300D (PerkinElmer, Inc., Waltham, MA, USA) inductively coupled plasma-mass spectrometer (ICP-MS). A total of 100 mg of sample powders were digested using HNO_3 + HF in a Teflon-lined vessel at 180 °C and 200 p.s.i. for 30 min, evaporation to dryness, and then subsequently dissolved in 100 mL of 4 vol% HNO_3. Both the XRF and the ICP-MS analyses were carried out at the Scientific Instruments Centre of the University of Granada (CIC-UGR, Spain).

Palaeoclimatic and palaeoweathering proxies (Ba/Sr, Sr/Cu, Ga/Rb, and Rb/Sr) were calculated from the chemical analyses of the iron crust from the Villas section and the chemical analyses reported by Reolid et al. [32] for the iron crust in the RGCH section to infer the palaeoclimatic conditions.

To evaluate the degree of chemical weathering in the iron crust from the Villas section and those reported in the RGCH and PC2 sections [21,32], the Chemical Index of Alteration (CIA) and the Chemical Index of Weathering (CIW) were determined. These indexes were calculated by adapting the formula proposed by Nesbitt and Young [57]:

$$CIA = [Al_2O_3 / (Al_2O_3 + Na_2O + K_2O)] \times 100 \tag{1}$$

and the formula proposed by Harnois [58]:

$$CIW = [Al_2O_3 / (Al_2O_3 + Na_2O)] \times 100 \tag{2}$$

The CaO values are not considered in these calculations since, as will be shown later, they come from the small proportions of calcite present in the crusts and not from the phyllosilicates.

Additionally, the palaeoprecipitation regime was calculated using the climofunctions of Sheldon et al. [59].

$$P = 221 \, e^{0.0197(\text{CIA-K})} \tag{3}$$

$$P = 14.265 \, (\text{CIA-K}) - 37.632 \tag{4}$$

$$P = -259.34 \ln (B) + 759.05 \tag{5}$$

where *P* is the palaeoprecipitation (mm/yr) and *B* in Equation (5) is the molecular ratio of $CaO + MgO + Na_2O$ to Al_2O_3 [59].

4. Results

4.1. Sedimentary Features

In the Villas section, the boundary between the Middle and Upper Jurassic is represented by a reddish terrigenous iron crust containing iron-coated grains (Figure 2). This crust is harder than the crust described in the other sections from the Central External Prebetic. According to Reolid and Abad [21], the iron crust is poorly preserved in the Prebetic. When preserved, it is a hard crust ranging from 2 to 10 cm in the Central Prebetic of Sierra de Cazorla (RGCH section). This crust is represented by a soft reddish to yellowish crust in the Eastern Prebetic (PC2 section), but commonly, it is not recorded or millimetric (PC 1 section). The iron crust related to the Middle–Upper Jurassic discontinuity has not been recorded in the Iberian Range.

Over the iron crust, and commonly, directly overlying the Middle Jurassic carbonates, there is the ferruginous oolithic limestone both in the External Prebetic and the Iberian Range [19,21,31,46]. Iron-coated grains are commonly recorded in these lithofacies together with abundant fossil remains such as ammonoids and belemnites that indicate the Middle Oxfordian Plicatilis Zone [31]. Over the ferruginous oolithic limestone, there are spongiolithic limestones with their lower part dated as Middle Oxfordian (Transversarium Zone) [31] (Figure 2).

In the Villas section, the iron crust is followed by a yellow ferruginous–carbonated breccia containing iron-coated grains (Figure 2) as well as a wide range of sedimentary rock fragments with different textures. This breccia does not occur in the other sections described in the External Prebetic [21,32] (Figure 2). There are no fossils of ammonoids and belemnites in the breccia of the Villas section. This lithofacies constituted a clear difference with respect to the rest of the studied outcrops. Over this lithofacies, there are spongiolithic limestones, the lower part of which dated to the Middle Oxfordian (Transversarium Zone). The age of the ferruginous–carbonated breccia is probably the same as the ferruginous oolithic limestone (Plicatilis Zone).

4.2. The Iron Crust Containing Iron-coated Grains

4.2.1. Mineralogical Composition

The XRD pattern of the whole rock and the calculated relative proportions indicate that the iron crust from the Villas section is mainly composed of clay minerals (44%), quartz (35%), and goethite (11%), together with minor proportions of calcite, dolomite, orthoclase and hematite (<5%) (Figure 3a).
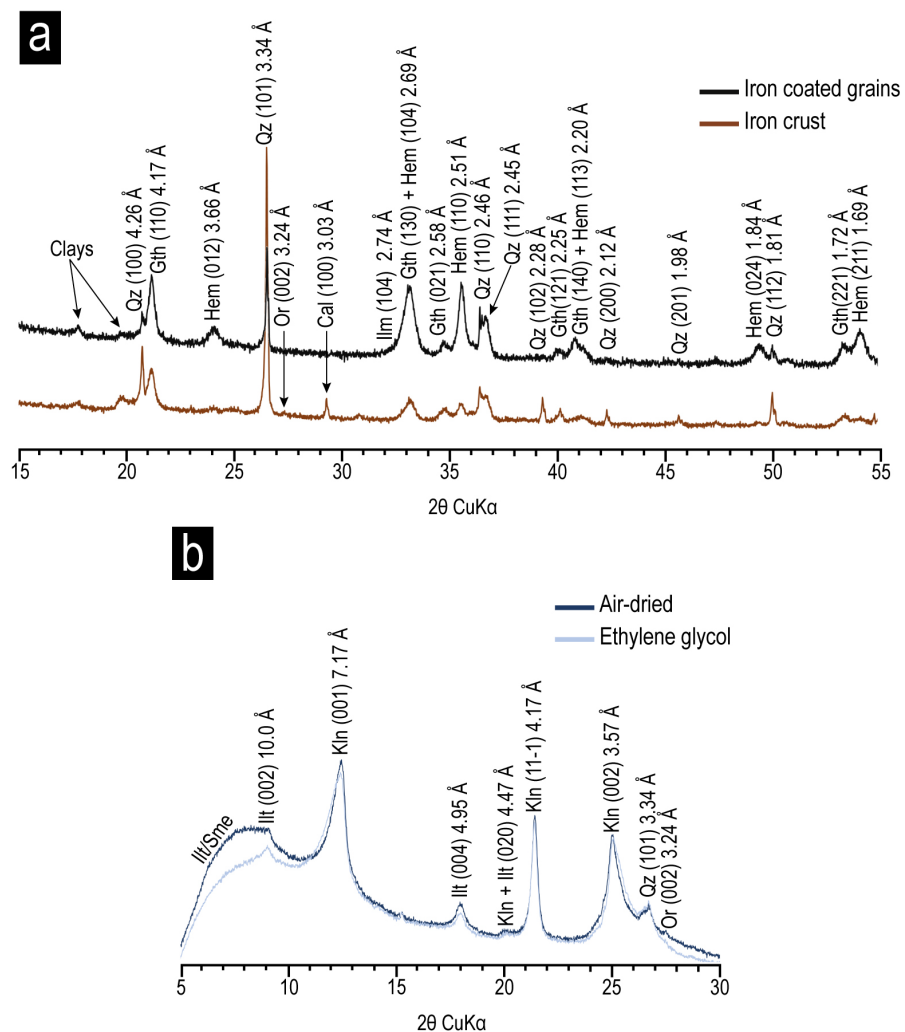
Figure 3. (**a**) XRD patterns obtained from the whole rock of the iron crust and the iron-coated grains from the Villas section; (**b**) XRD patterns obtained from the <2 μm fraction of the iron crust from the Villas section. *Clays* = clay minerals, *Qz* = quartz, *Gth* = goethite, *Hem* = hematite, *Or* = orthoclase, *Cal* = calcite, *Ilm* = ilmenite, *Ilt/Sme* = illite/smectite mixed layers, *Ilt* = illitic phases, *Kln* = kaolinite.

In the <2 μm fraction, abundant kaolinite (43%) and illitic phases (57%) are identified in the XRD pattern of the iron crust from the Villas section. Characteristic reflections of kaolinite at 7.15, 4.18, and 3.57Å are identified, and dickite and nacrite reflections are not detected. Illite and micas (quantified together) are included within the term "illitic phases", as well as random mixed-layer illite/smectite (Ilt/Sme), which were not quantified but were detected in the XRD pattern (Figure 3b).

The XRD patterns of the iron-coated grains included in the crust from the Villas section show that they are mainly composed of 34% of clay minerals (mainly kaolinite as deduced by SEM study), 23% of goethite, 23% of quartz, 10% of ilmenite, and 9% of hematite (Figure 3a).

According to the method proposed by Schulze [54] for determining the Al^{3+} content in the goethite structure, based on the position of de d_{110} and d_{111} peaks of this mineral phase, thereis an Al-substitution in goethite of 13% mol in the iron crust and of 7% in the iron-coated grains from the Villas section.

4.2.2. Textural Features

The optical microscopy images show that the iron crust from the Villas section is formed by a fine-grained matrix containing clay minerals and iron oxides whose small

size did not allow their identification under optical microscopy resolution (Figure 4a). Abundant quartz grains (300 μm–1 mm) are differentiated within the matrix (Figure 4b).
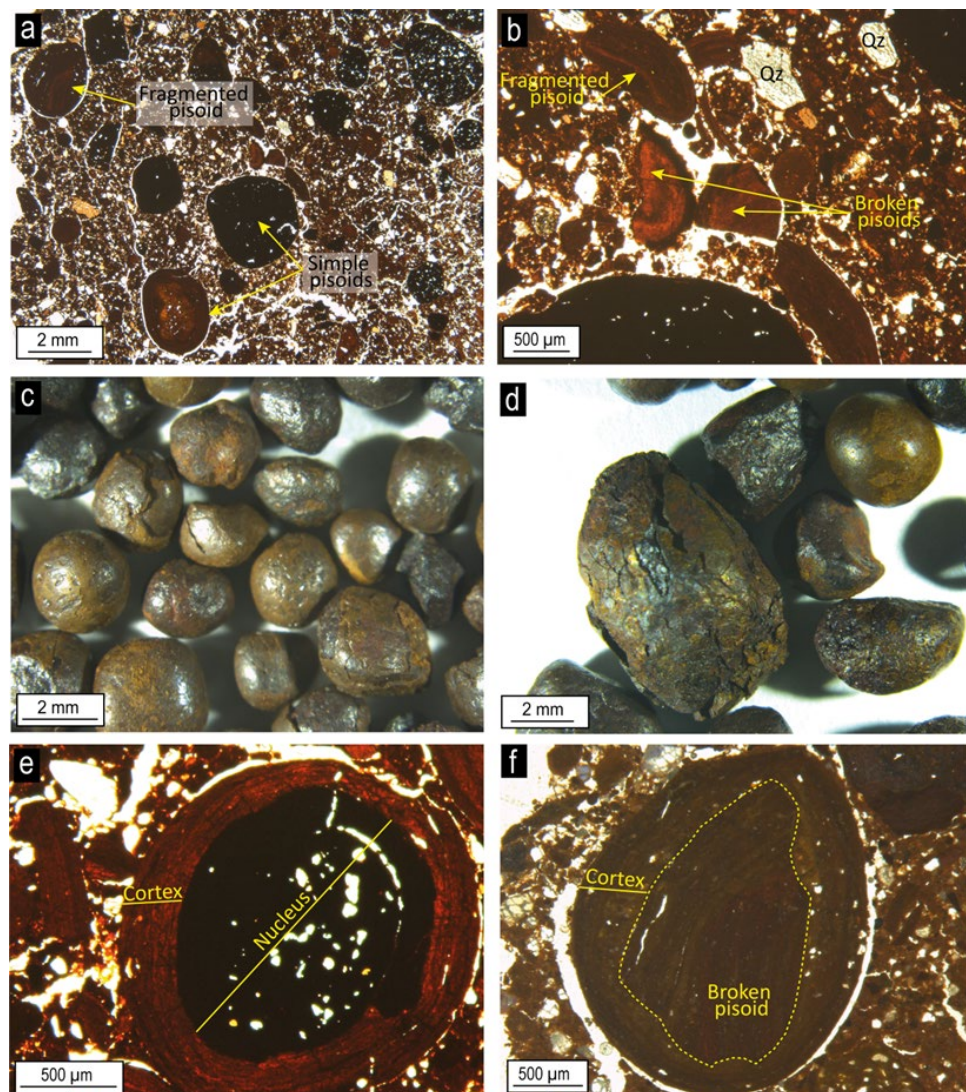

Figure 4. Optical microscopy (**a**,**b**,**e**,**f**) and binocular loupe (**c**,**d**) images of the iron crust containing iron-coated grains from the Villas section: (**a**) Simple and fragmented pisoids in the clay-rich matrix of the crust; (**b**) Fragmented pisoids, broken pisoids, and quartz clasts in the clay-rich matrix of the crust; (**c**,**d**) Spherical to ellipsoidal pisoids and macropisoids extracted from the crust; (**e**) Simple pisoid showing a nucleus composed by an indeterminate ferruginous lump and a cortex formed by several concentric layers; (**f**) fragmented pisoid whose nucleus is a broken pisoid. *Qz* = quartz.

The iron-coated grains included in the iron crust from the Villas section are spherical to ellipsoidal with sizes from 300 μm to 7 mm, encompassing macropisoids, pisoids, and ooids according to Bárdossy [55], being the pisoids the predominant ferruginous particles in the crust (Figure 4c). These ferruginous particles are included in the type A category of the iron-coated grains proposed by Reolid et al. [32] based on morphology and internal microstructure. According to these authors, type A iron-coated grains are constituted by a thin and regular lamination, forming concentric layers around a nucleus. The nuclei of the macropisoids, pisoids, and ooids from the Villas section are formed by an indeterminate ferruginous lump or by a fragment of a previously broken iron-coated grain, which allows them to be classified as simple and fragmented pisoids, according to Guerrak [60] classification (Figure 4a,b,e,f). The nucleus and the cortex (formed by concentric layers) of

the simple pisoids are composed of a mixture of clay minerals, iron oxides, and occasional quartz grains. Some simple pisoids are broken and can act as a nucleus for the fragmented pisoids (Figure 4b,f). The fragmented pisoids also present several concentric layers with the same composition as those of the simple pisoids (Figure 4f).

Backscattered and secondary electron images of the iron crust from the Villas section show a clay-rich matrix formed by kaolinite and iron oxides (hematite and goethite as detected by XRD) (Figure 5a–c). Quartz grains with anhedral morphologies are also observed (Figure 5a). Kaolinite crystals appear as subhedral to euhedral nanometric plates (100 nm–1 μm), showing pseudohexagonal outlines with random orientation, as well as forming book-type aggregates (Figure 5a,b). The illitic phases are larger than kaolinite crystals (5–10 μm) and present subhedral morphologies with their sheets frequently separated (Figure 5c). Nanometric kaolinite crystals growing over illitic plates are also observed (Figure 5d).
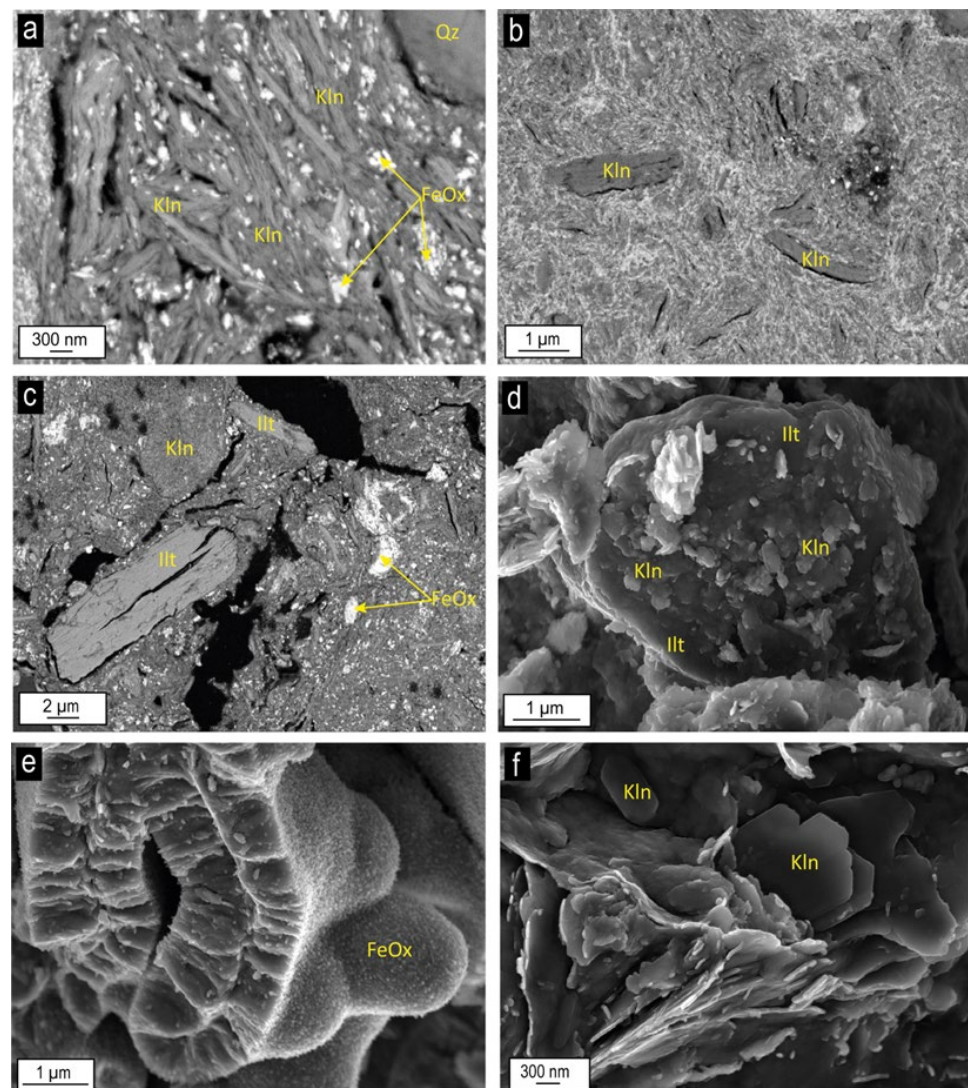
Figure 5. SEM images of the iron crust from the Villas section (**a–d**) and the iron crust from the PC2 section (**e**,**f**) showing: (**a**) a mixture of nanometric kaolinite plates and nanometric iron oxides forming the matrix of the crust; (**b**) nanometric to micrometric kaolinite booklets in the matrix of the crust; (**c**) micrometric subhedral illitic phases showing their sheets separated; (**d**) nanometric pseudohexagonal kaolinite plates over micrometric subhedral illitic phases; (**e**) tube-like filaments composed by nanometric acicular iron oxides; (**f**) nanometric pseudohexagonal kaolinite plates with random orientation. *FeOx* = iron oxides, *Kln* = kaolinite, *Qz* = quartz, *Ilt* = illitic phases.

The new analysis of the secondary electron images of the iron crust from the PC2 section shows areas with nanometric iron oxide crystals forming tube-like filaments (~1 μm in diameter) (Figure 5e), as well as areas with nanometric kaolinite crystals with subhedral shapes (Figure 5f).

The nucleus and the cortex of the iron-coated grains embedded in the clay-rich matrix of the iron crust from the Villas section are mainly composed of hematite and goethite with different proportions of kaolinite (Figure 6). Kaolinite presents the same morphological features as those observed in the clay-rich matrix of the iron crust, forming subhedral nanometric plates with random orientation, as well as book-type aggregates (Figure 6a,b). Some of the kaolinite book-type aggregates present iron oxide crystals between their sheets (Figure 6b). In addition, the concentric layers that form the cortex of the iron pisoids contain different amounts of kaolinite and iron oxides, allowing the different layers to be differentiated (Figure 6c,d).
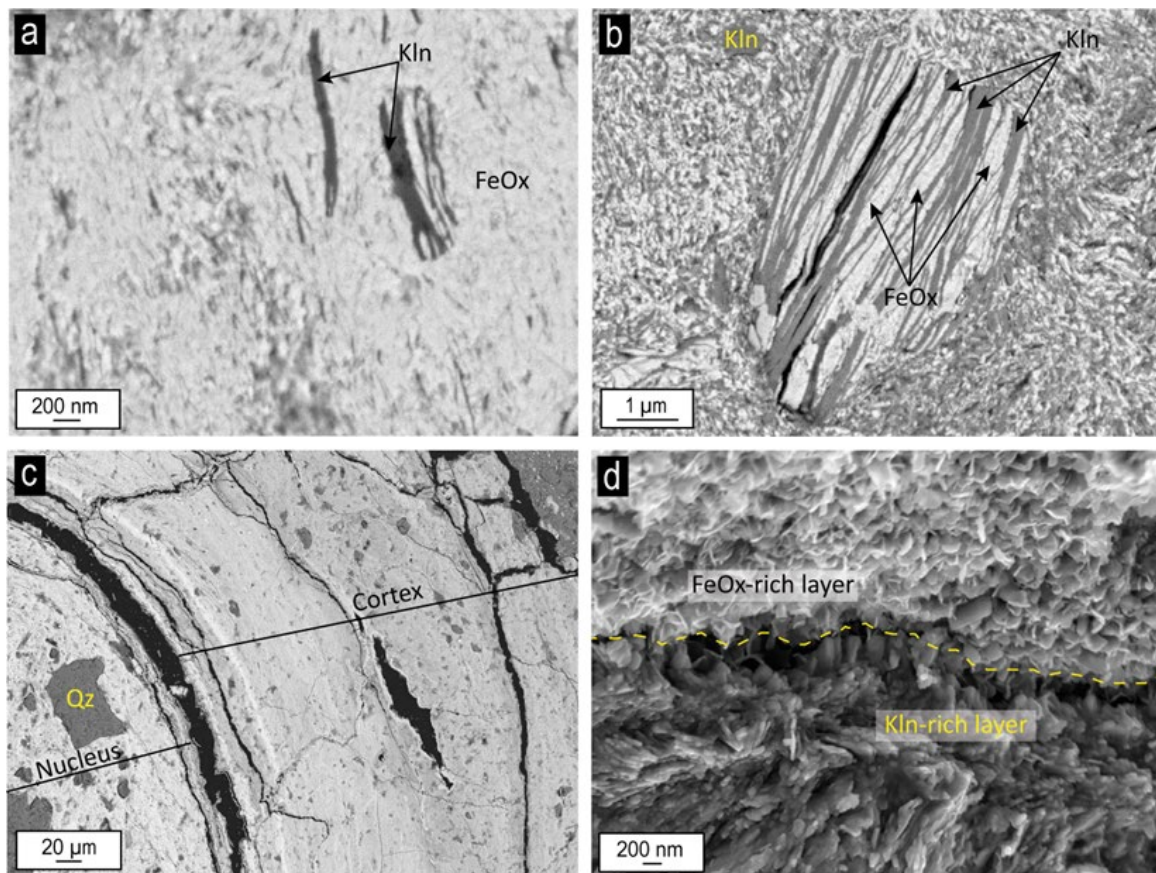
Figure 6. SEM images of the iron-coated grains in the iron crust from the Villas section showing: (**a**,**b**) nanometric kaolinite plates and iron oxides, with iron oxides occasionally growing between the kaolinite plates; (**c**) the nucleus and the cortex of a simple pisoid both composed by different proportions of iron oxides and kaolinite; (**d**) the cortex of a simple pisoid where two layers can be differentiated by their higher content in fibrous iron oxides crystals or kaolinite plates. *Kln* = kaolinite, *FeOx* = iron oxides, *Qz* = quartz.

4.2.3. Geochemical Composition

The geochemical composition of major and minor elements of the matrix of the iron crust and the iron-coated grains from the Villas section is represented in Tables 1 and 2. The geochemical composition of the previously analyzed iron crusts and iron-coated grains from the Prebetic reported by Reolid and Abad [21] and Reolid et al. [32] are also included in Tables 1 and 2 for comparison with the new data from the Villas section.

Table 1. Major element contents (wt.%) of the iron crust and the iron-coated grains obtained for the Villas section and those reported by Reolid and Abad [21] and Reolid et al. [32] for the iron crusts of the RGCH and PC2 sections and the iron-coated grains from the RGCH section. The obtained values for the CIA and CIW indexes calculated from all the iron crusts are also included, as well as the palaeoprecipitation regime (PPR) (mm/yr) obtained from the average of Formulae 3–5.

	Iron Crust			Iron-Coated Grains	
	Villas	**RGCH**	**PC2**	**Villas**	**RGCH**
SiO_2	39.33	3.84	11.95	11.70	5.39
Al_2O_3	12.91	2.52	5.41	7.32	6.47
Fe_2O_3	31.06	80.48	71.19	72.70	67.28
MnO	0.07	0.03	0.04	0.08	0.05
MgO	0.67	0.33	0.27	0.10	0.52
CaO	2.19	2.31	1.89	0.25	4.69
Na_2O	0.06	-	0.12	0.03	-
K_2O	0.51	0.10	0.31	0.02	0.24
TiO_2	0.88	0.14	0.56	0.62	0.53
P_2O_5	0.09	1.76	0.49	0.03	3.58
LOI	12.15	10.88	7.45	5.78	6.45
CIA	95.20	95.87	90.87	-	-
CIW	91.99	93.59	88.14	-	-
PPR	1380.20	1329.00	1325.06	-	-

Table 2. Trace element contents (ppm) of the iron crust and the iron-coated grains obtained for the Villas section and those reported by Reolid et al. [32] for the iron crust and the iron-coated grains for the RGCH section. The Ba/Sr, Sr/Cu, Rb/Sr, and Ga/Rb ratios calculated from these analyses are also included.

	Iron Crust		Iron-Coated Grains	
	Villas	**RGCH**	**Villas**	**RGCH**
Li	67.00	-	35.12	-
Rb	24.64	5.15	2.04	10.36
Cs	2.49	0.41	0.40	0.81
Be	5.44	-	6.79	-
Sr	22.43	44.53	14.90	65.86
Ba	80.4	27.29	34.50	51.69
Sc	23.05	14.23	25.60	15.10
V	424.02	1414.42	1067.87	1908.24
Cr	154.44	186.09	280.63	1058.94
Co	30.14	143.36	39.61	121.09
Ni	65.4	384.68	72.49	369.06
Cu	36.85	54.94	39.79	35.25
Zn	20.78	289.60	9.44	311.37
Ga	37.39	7.44	41.61	13.44
Y	88.14	66.28	80.87	107.45
Nb	14.87	9.57	11.72	40.42
Ta	1.33	0.31	0.87	1.02
Zr	168.66	62.52	125.25	147.71
Hf	4.76	1.39	3.23	4.31
Mo	2.69	56.07	8.18	10.18
Sn	3.8	0.64	2.58	3.01
Tl	0.18	0.13	0.06	0.56
Pb	59.67	150.74	139.22	120.89
U	2.87	13.17	4.74	8.02
Th	22.4	6.97	26.54	27.87
La	134.42	29.58	107.02	55.09
Ce	211.29	13.79	146.33	31.30

Table 2. *Cont.*

	Iron Crust		Iron-Coated Grains	
	Villas	**RGCH**	**Villas**	**RGCH**
Pr	32.58	4.42	25.92	10.38
Nd	128.71	19.03	104.25	43.83
Sm	28.15	4.09	24.51	10.35
Eu	6.49	0.95	5.98	2.30
Gd	20.62	5.13	18.20	11.09
Tb	2.88	0.87	2.52	1.81
Dy	12.67	5.76	14.16	12.07
Ho	2.86	1.41	2.84	2.67
Er	6.45	4.01	6.95	7.14
Tm	0.86	0.60	0.97	1.06
Yb	4.87	3.47	5.39	6.02
Lu	0.74	0.55	0.78	0.83
Ba/Sr	3.58	0.61	0.67	0.23
Sr/Cu	0.61	0.81	0.37	1.87
Rb/Sr	1.10	0.12	0.14	0.16
Ga/Rb	1.52	1.45	20.40	1.28

The content in major elements of the matrix of the iron crust from the Villas section (Table 1) fits well with the mineralogy detected by XRD, showing high contents in Fe_2O_3 (31.06%), SiO_2 (39.33%) and Al_2O_3 (12.92%), reflecting the high presence of clay minerals (kaolinite and illitic phases), as well as goethite. In the case of the iron crust from the RGCH and PC2 sections, their higher Fe_2O_3 content (80.4% and 71.19%, respectively), reflects the higher presence of hematite and goethite. The higher content of P_2O_5 (1.75%) in the RGCH iron crust (0.07%–0.48%) also reflects the presence of apatite reported by Reolid et al. [32]. In addition, the CaO content in all the crusts correlates with calcite content. The iron crusts from the Villas, RGCH, and PC2 sections contain minor proportions of calcite, which is reflected in their lower CaO content (2.19%, 2.31%, and 1.89%, respectively). For this reason, CaO content was not considered when calculating CIA and CIW indexes.

The iron-coated grains included in the iron crust from the Villas section show higher Fe_2O_3 (72.70%) and lower Al_2O_3 (7.32%) and SiO_2 (11.70%) contents than the iron crust, reflecting the higher presence of goethite with respect to clay minerals. According to the Fe_2O_3-Al_2O_3-SiO_2 diagram of Aleva [61], the iron crust from the RGCH and PC2 sections can be classified as ferrites, whereas the iron crust from the Villas section, plots on the kaolinite field but closer to the laterite field (Figure 7a).

Weathering trends are represented using the Fe_2O_3 + MgO-CaO + Na_2O + MgO-Al_2O_3 diagram of Mitchell and Sheldon [62] and the Al_2O_3-CaO + Na_2O-K_2O diagram of Nesbit and Young [63] (Figure 7b,c). The CaO + Na_2O + MgO content is low in all the iron crusts, whereas Fe_2O_3 + MgO content is higher in the RGCH and PC2 sections, and Al_2O_3 content is higher in the Villas section (Figure 7b). The bedrock of the iron crust from the Villas section has a high degree of disintegration to soil compared to that of the iron crust from the RGCH and PC2 sections (Figure 7c).

The calculated CIA and CIW values are higher in the iron crust from the RGCH (CIA = 95.87, CIW = 93.58) and Villas (CIA = 95.20, CIW = 91.99) sections than in the iron crust from the PC2 section (CIA = 90.89, CIW = 88.14). In the same way, the palaeoprecipitation regime is higher in the Villas (1380.20 mm/yr) and RGCH (1329.00 mm/yr) sections than in the PC2 section (1325.06 mm/yr).
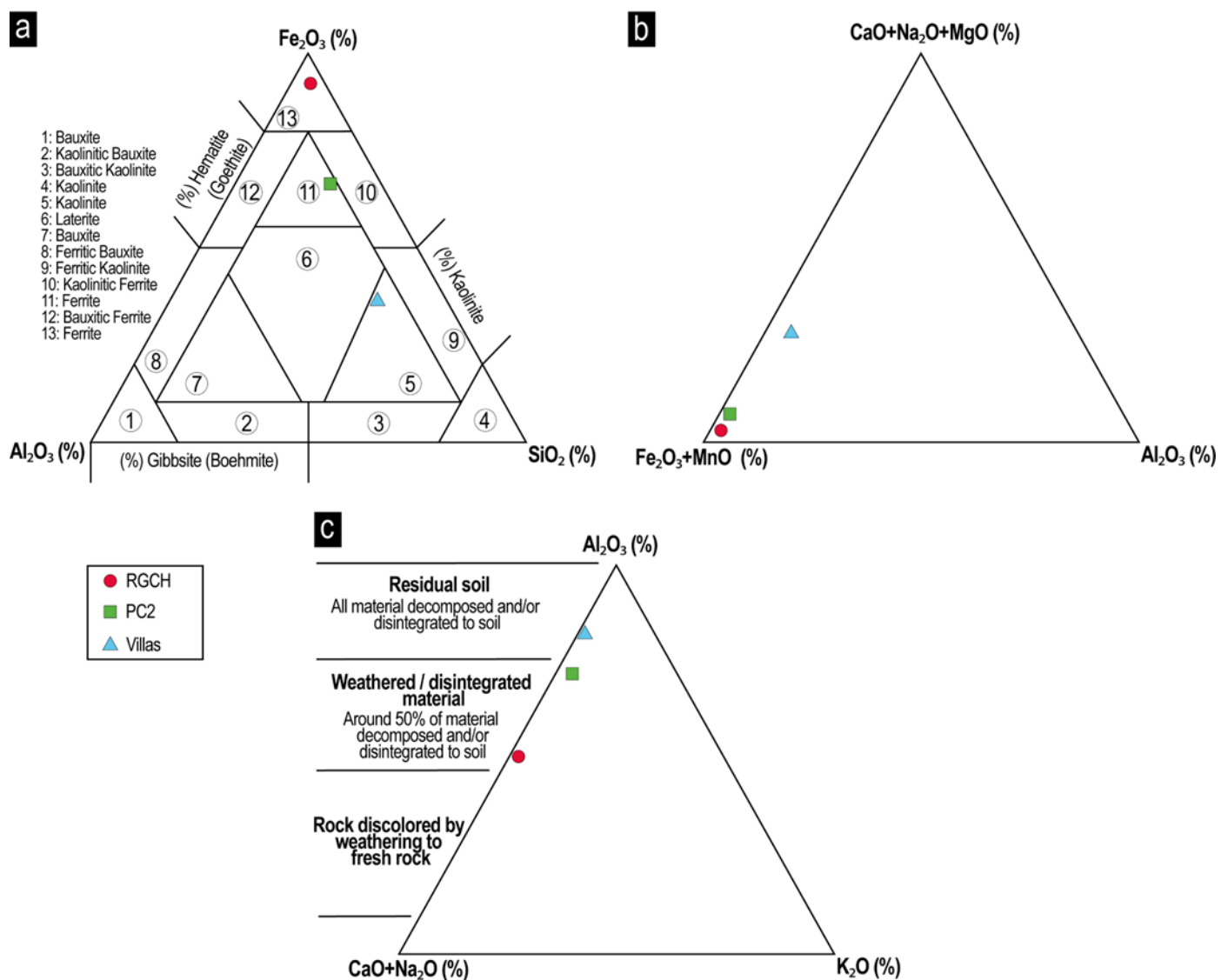
Figure 7. Ternary diagrams showing the geochemical composition of the iron crusts from the Villas, RGCH, and PC2 sections: (**a**) Fe_2O_3-SiO_2-Al_2O_3 diagram of bauxite chemical classification [61]; (**b**) Fe_2O_3 + MgO-CaO + Na_2O + MgO-Al_2O_3 diagram of Mitchell and Sheldon [62]; (**c**) Al_2O_3-CaO + Na_2O-K_2O diagram of Nesbit and Young [63]. The geochemical data of the RGCH and PC2 sections have been taken from Reolid et al. [32] and Reolid and Abad [21], respectively.

With respect to the trace element content (Table 2), the Ba/Sr, Sr/Cu and Rb/Sr ratios of the iron crust from the Villas section are higher (Ba/Sr$_{crust}$ = 3.58, Sr/Cu$_{crust}$ = 0.61 and Rb/Sr$_{crust}$ = 1.10) than those calculated for the iron-coated grains included in the crust (Ba/Sr$_{grains}$ = 0.67, Sr/Cu$_{grains}$ = 0.37 and Rb/Sr$_{grains}$ = 0.14). In the RGCH section, the Ba/Sr ratio is higher in the crust (0.61) than in the iron-coated grains (0.23), whereas the opposite occurred for the Sr/Cu and Rb/Sr ratios, which are higher in the iron-coated grains (Sr/Cu$_{grains}$ = 1.87 and Rb/Sr$_{grains}$ = 0.16) than in the crust (Sr/Cu$_{crust}$ = 0.81 and Rb/Sr$_{crust}$ = 0.12). The Ga/Rb ratios obtained for the Villas (Ga/Rb$_{crust}$ = 1.52 and Ga/Rb$_{grains}$ = 20.40) and the RGCH (Ga/Rb$_{crust}$ = 1.45 and Ga/Rb$_{grains}$ = 1.28) sections show similar values for the crusts but a clear much higher Ga/Rb ratio value in the iron-coated grains from the Villas section.Comparing the iron crusts and the iron-coated grains chondrite-normalized patterns to the bulk composition of the upper continental crust (Post-Archean Australian Shales, PAAS) of Taylor and McLennan [64], it can be observed that both the iron crust and the iron-coated grains from the Villas section are enriched in

LREE and HREE (Figure 8a). By contrast, a relative impoverishment in LREE but a slight enrichment in HREE occur in the crust from the RGCH section, whereas, except for Ce, the iron-coated grains are enriched in REE, according to the data reported by Reolid et al. [32] (Figure 8a). The REE fractionation is higher in the Villas section than in the RGCH section, this fractionation being higher in the crust than in the pisoids (Figure 8b,c). The iron crusts and the iron-coated grains of both sections show negative Eu and Ce anomalies, which are weaker in the Villas section (Figure 8).
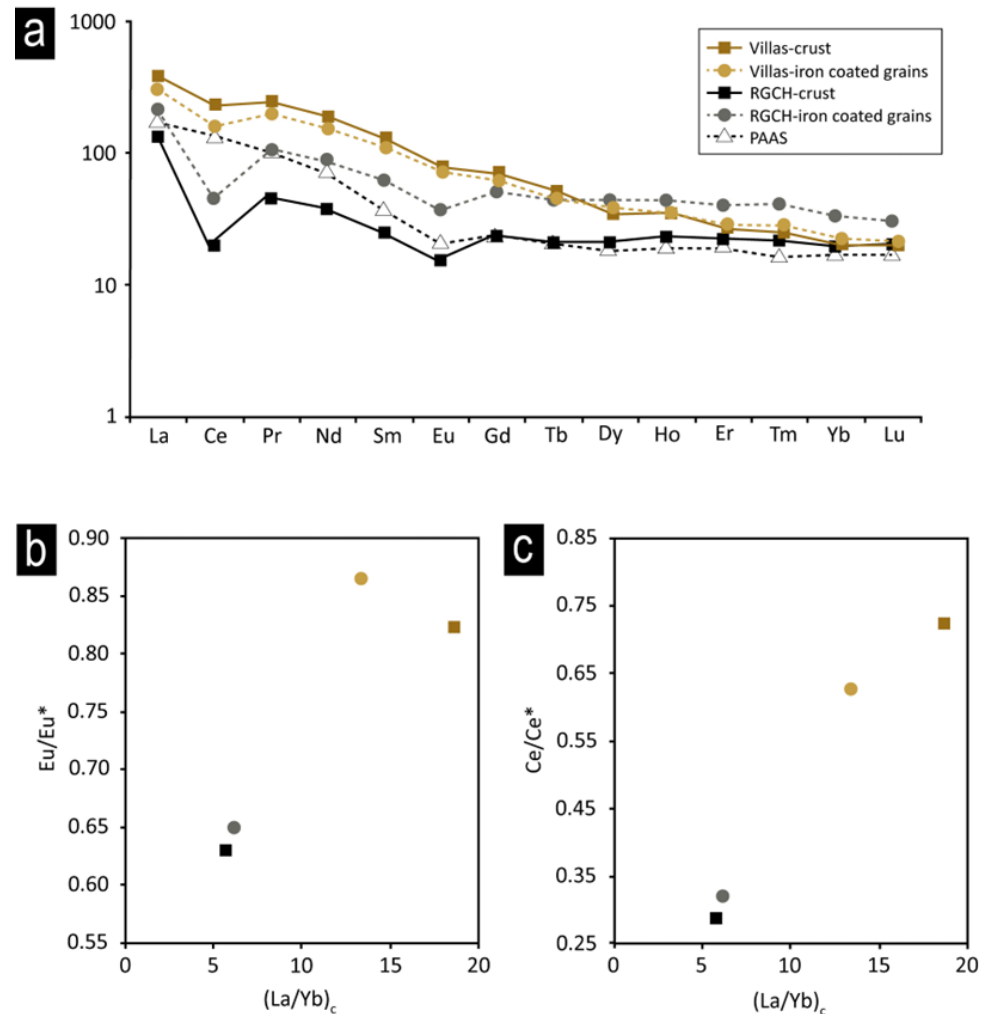

Figure 8. (**a**) Chondrite-normalized REE patterns of the crusts and the iron-coated grains from the Villas and RGCH sections; (**b**,**c**) plot of the Eu/Eu* and Ce/Ce* vs. (La/Yb)$_c$ values, respectively, in the crusts and the iron-coated grains from the Villas and RGCH sections. The subscript *c* refers to those values normalized to chondrite. The geochemical data of the RGCH section have been taken from Reolid et al. [32].

4.3. The Iron-Coated Grains of the Ferruginous–carbonated Breccia and the Ferruginous Oolithic Limestones

4.3.1. Textural Features

In the ferruginous–carbonated breccia of the Villas section, iron-coated grains and micritic clasts cemented by sparite are observed (Figure 9a). The iron-coated grains present the same textural features as those embedded in the clay-rich matrix of the iron crust, which has a range from 200 μm to 7 mm, encompassing iron macropisoids, pisoids, and ooids according to Bárdossy [55], being pisoids the most common ones. They are included in the type A category of Reolid et al. [32], differentiating simple and fragmented pisoids

(Figure 9b). The nucleus and the cortex are also composed of a mixture of clay minerals, iron oxides, and occasional quartz grains (Figure 9c,d).
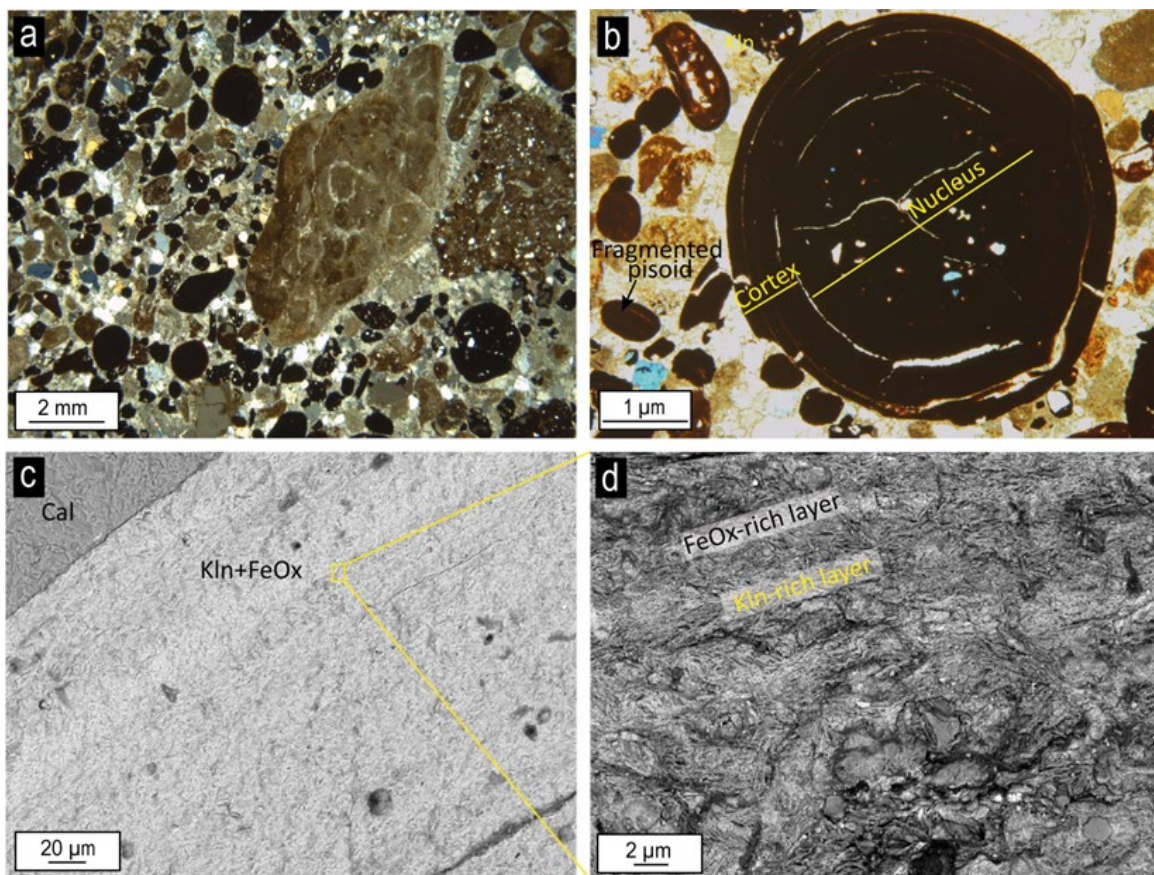
Figure 9. Optical microscopy (**a**,**b**) and SEM (**c**,**d**) images of the ferruginous–carbonated breccia from the Villas section showing: (**a**) iron-coated grains and micritic clasts in a sparite matrix; (**b**) simple and fragmented pisoids in the sparite matrix; (**c**,**d**) the cortex of a simple pisoid where the different layers can be differentiated by their higher content in iron oxides or kaolinite. *Cal* = calcite, *Kln* = kaolinite, *FeOx* = iron oxides.

In the ferruginous oolithic limestone from the RGCH, CHO and PC1 sections and the equivalent lithofacies of the AF section, iron-coated grains are found embedded in a micritic-sparitic matrix. Following the classifications given by Reolid et al. [32] and Guerrak [60], these iron-coated grains are included within type A and type B (Figure 10). Unlike the iron crust and the ferruginous–carbonated breccia from the Villas section, the four morphological types of type A iron-coated grains are found in the RGCH, CHO, and PC1 sections and in the AF section (Figure 10): simple, fragmented, complex and spastolith. Simple and fragmented pisoids are the most frequent particles and present the same morphological features as those found in the iron crust and the ferruginous–carbonated breccia from the Villas section (Figure 10a,d,e). Complex pisoids, although scarcer, can be observed as being formed by two or more nuclei composed of indeterminate ferruginous lumps evolved by several concentric layers (Figure 10b). Spastoliths, which are distorted and stretched iron-coated grains deformed by squashing [32], are more frequent than complex pisoids and present distorted and stretched grains (Figure 10c). The type B iron-coated grains can be classified as simple and complex, formed by one or two nuclei composed by a previous iron ooid, bioclast, foraminifera, or quartz grains (Figure 10f).
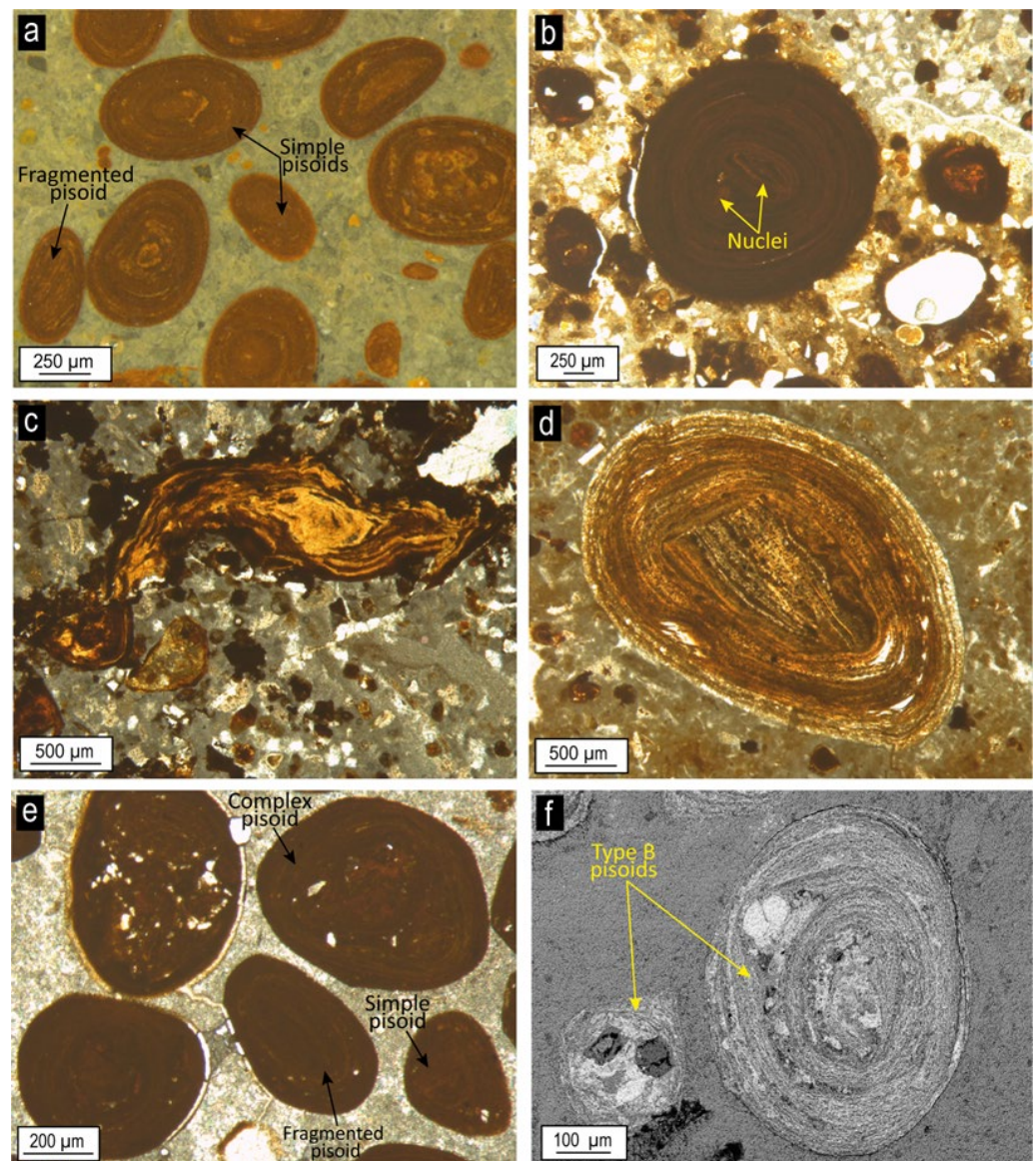
Figure 10. Optical microscopy (**a**–**e**) and SEM (**f**) images of the ferruginous oolithic limestones from the RGCH, CHO and PC1 sections (**a**–**d**) and the AF section (**e**–**f**) showing: (**a**,**d**,**e**) type A iron-coated grains including simple and fragmented pisoids; (**b**,**e**) complex type A iron-coated grains; (**c**) spastoliths; (**f**) simple (right) and complex (left) type B iron-coated grains.

4.3.2. Geochemical Composition

The EDS compositional maps of different iron-coated grains embedded in the iron crust and the ferruginous–carbonated breccia (Villas section) and in the ferruginous oolithic limestone (AF section) are represented in Figure 11. Those from the Villas section correspond to type A simple pisoids, composed of a nucleus and a more or less developed cortex, whereas the pisoids from the AF section are type B simple pisoids, which present two types of nuclei (a previous iron ooid and a foraminifera) and a cortex made up of several concentric layers. Regardless of the pisoid type, all the EDS elemental maps show that both the nucleus and the cortex are composed of a mixture of Al and Fe due to the presence of kaolinite, hematite, and goethite. In the more developed cortexes (Figure 11b,c), different content of Al and Fe are observed, allowing one layer to be differentiated from the other in both type A and type B simple pisoids. However, the compositional maps show clearly that the lamination of type A pisoids is thinner and less irregular than in type B.
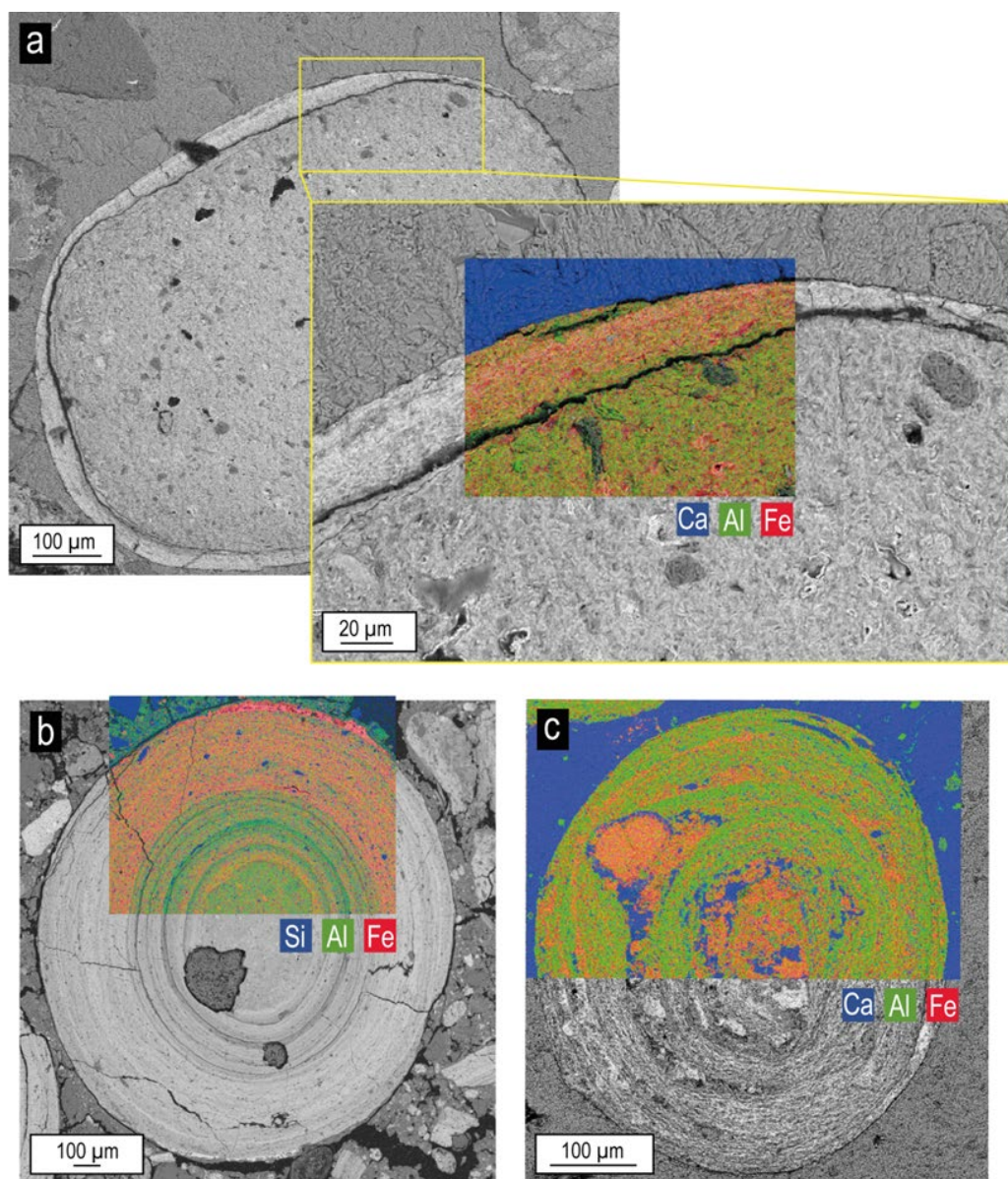
Figure 11. EDS compositional maps over SEM images of: (**a**) type A iron-coated grain (simple pisoid) in the ferruginous–carbonated breccia from the Villas section; (**b**) type A iron-coated grain (simple pisoid) in the iron crust from the Villas section; (**c**) type B iron-coated grain (simple pisoid) in the ferruginous oolithic limestone from the AF section.

XRF compositional maps of the ferruginous–carbonated breccia from the Villas also reveal that some metals, such as Ba, Co, Mn, Ti, and Cr, are concentrated in certain layers of the iron-coated grains (Figure 12). Ba and Ti are concentrated in the nucleus and some layers, coinciding with those areas where Si and Al contents are higher. By contrast, the Co, Cr, and Mn distribution within the iron-coated grains coincides with higher Fe contents (Figure 12).
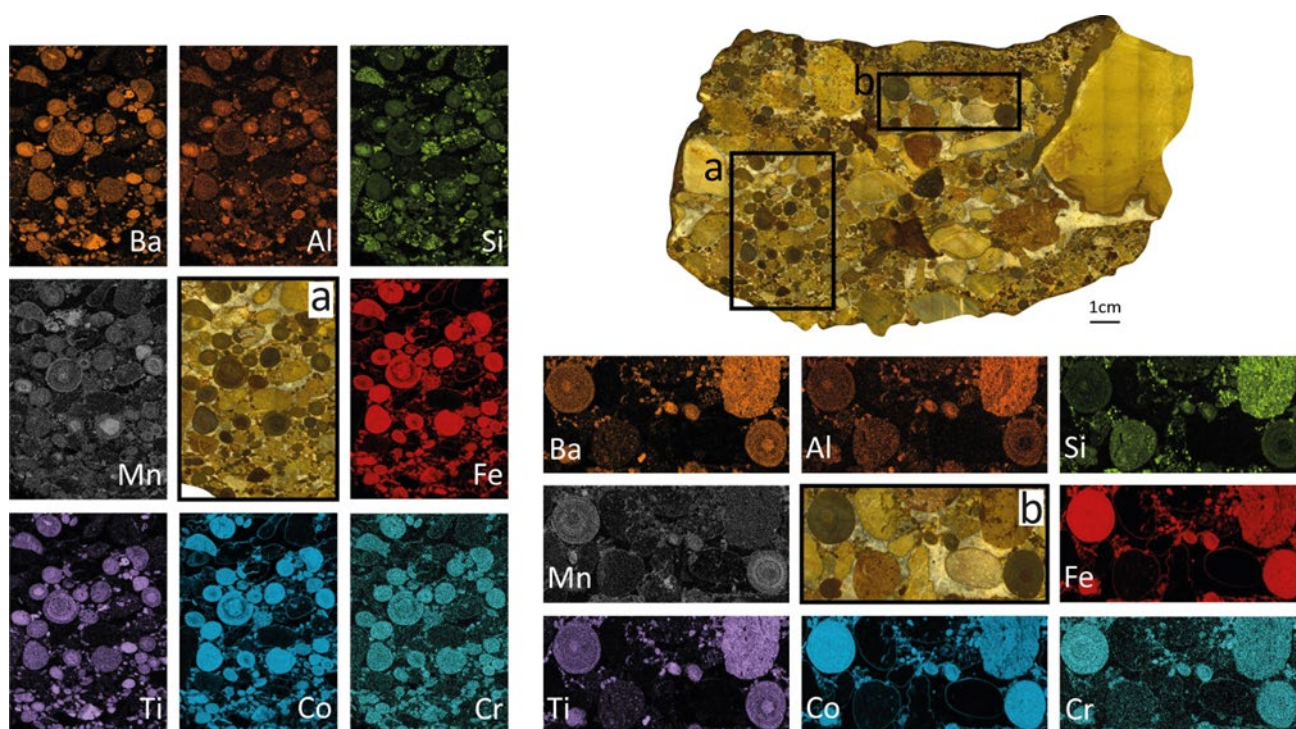
Figure 12. X-ray microfluorescence elemental maps of the ferruginous–carbonated breccia from the Villas section that allows us to observe differences in the distribution of elements in function of their affinities for Fe or Si-Al.

5. Discussion

5.1. Genesis of the Iron Crusts Containing Iron-Coated Grains

The electron microscopy images provide key textural and compositional information of the clay minerals for the interpretation of their origin. The euhedral to subhedral kaolinite plates showing pseudohexagonal outlines and the type-book aggregates, which are mixed with the iron oxides in the matrix of the iron crust from the Villas section, are indicative of an authigenic origin since these textures are too delicate to withstand erosion or transport processes [8,11,65]. Platy kaolinites and booklets have commonly been described as the result of chemical weathering processes during soil development [3,6–11]. In this way, kaolinite would have thus crystallized during edaphic processes after the dissolution of previous aluminosilicates present in the parent rock (e.g., orthoclase and illitic phases).

These genetical conditions are not compatible with the formation of illitic phases, which are commonly associated with diagenetic or hydrothermal environments [9]. In those environments, kaolinite would destabilize from 95–120 °C [66–68]. In addition, the genesis of Ilt/Sme from illite degradation due to K loss has also been described during chemical weathering processes [13,69–71].

Kaolinite has been observed over subhedral illitic phase plates, which may indicate that the illitic phases are earlier phases that acted as substrates for kaolinite crystallization, as described in other palaeosols and sediments [6,72]. Therefore, the illitic phases would probably have a detrital origin and may destabilize during the soil development, giving place to the genesis of kaolinite and Ilt/Sme mixed layers.

Goethite and hematite form the matrix of the iron crust together with the clay minerals, which also suggests an edaphic origin for these minerals [65,73]. On the other hand, quartz fragments showing anhedral morphologies reflect detrital phases that may represent the remains of the partial dissolution of the parent rock.

In the matrix of the iron crust from the PC2 section, iron oxide tube-like filaments are observed. The PC2 iron crust contains not only the iron oxide tube-like filaments but also subhedral kaolinite plates similar to those observed in the iron crust from the Villas section,

pointing out an edaphic origin for this crust. The iron oxide tube-like filaments observed in the PC2 section would have been generated during the soil development, most probably due to microorganisms as has been described in other palaeosols [74,75].

Szamatek et al. [76] classify iron pisoids according to the kaolinite/hematite ratio as kaolinitic, kaolinitic–hematitic, hematitic–kaolinitic, or hematitic. Kaolinitic–hematitic and hematitic–kaolinitic pisoids have been previously described as pisoids composed of a nucleus of kaolinite or hematite surrounded by a cortex of alternating kaolinite and hematite layers [73]. The kaolinite and hematite content of the iron-coated grains from the iron crust of the Villas section allows them to be categorized as kaolinitic–hematitic pisoids, which is also supported by the different kaolinite and iron oxide contents observed in the cortex that allowed the differentiation of the different concentric layers.

The presence of kaolinite, goethite, and hematite in the iron-coated grains showing the same textural features as those observed in the matrix of the iron crust, along with their concentric structure, is typical of the edaphic process [6,9,55,65,77]. Therefore, the iron-coated grains included in the iron crust from the Villas section were formed in situ during the development of the soils. The secondary and backscattered electron images also showed Fe oxides growing between kaolinite sheets in the iron-coated grains. The Fe oxides cementing kaolinite have also been described in Lower Cretaceous lateritic palaeosols from the SE Iberian Range by Laita et al. [9], suggesting that these oxides generated at a late stage during the edaphic process.

The genesis of iron-coated grains requires hydrous conditions with permanent groundwater saturation [55,78] and is related to dissolution and re-precipitation processes that are controlled by different factors (e.g., climatic conditions, chemical composition of the groundwater, etc.) [79].

A possible later decrease in the water level may favoured the reworking and fragmentation of some of the iron-coated grains, giving place to the broken pisoids that acted as nuclei for new pisoids. Reworking processes affecting the iron-coated grains in different episodes of soil development have also been described in other palaeosols and sediments [6,9,80,81].

5.2. Provenance of the Iron-Coated Grains Included in the Ferruginous–Carbonated Breccia and the Ferruginous Oolithic Limestones

Eustatic and tectonic factors influenced the Middle–Upper Jurassic unconformity, which is linked to extensional tectonic activity related to an advanced rifting stage, followed by an oceanization and expansion phase recording in the Tethyan Domain during the Middle–Late Oxfordian [36,82]. Some authors report a sea-level fall during the Middle–Late Jurassic transition [25,32,83], whereas, for other authors, it was a global sea-level rise period [26,84,85]. The evidence of palaeosols development in the studied sections of the Prebetic agrees with a sea-level fall during the Late Callovian–Early Oxfordian.

The presence of type A iron-coated grains in the ferruginous oolithic limestones from the RGCH, CHO and PC1 sections is explained by reworking during the erosion of the iron crusts [21,32]. These ferruginous oolithic limestones represent Late Jurassic flooding events of the Prebetic, which developed in a sedimentation context dominated by storms [36,40,86]. The flooding events extended to the emerged areas, giving place to the erosion of the palaeosols previously developed in the coastal plain [21]. According to Olóriz et al. [31], the ferruginous oolithic limestones in the External Prebetic represent complex lithofacies with high energy features that combine the presence of components coming from proximal settings (iron-coated grains with edaphic origin, quartz grains coming from emerged lands, and benthic foraminifera of shallow environments) and others coming from distal environments (ammonoids, belemnites and planktic foraminifera).

Recent studies have pointed out that iron-coated grains included in Proterozoic oolithic ironstones formed by synsedimentary reworking processes in low-energy coastal environments [87]. According to these authors, negative Eu anomalies (as those reported by Reolid et al. [32] for the RGCH section) suggest a continental iron source. The iron-rich

microenvironment generated due to the redistribution of the iron crust fragments and type A iron-coated grains allowed the development of new iron-coated grains with marine features (type B iron-coated grains) in the ferruginous oolithic limestones [32].

On the other hand, a ferruginous–carbonated breccia containing juts type A iron-coated grains is recorded, instead of the ferruginous oolithic limestone, in the Villas section. The textural features and chemical and mineralogical composition of type A iron-coated grains from this ferruginous–carbonated breccia is similar to that observed in the iron crust. Therefore, these iron-coated grains might have been reworked from the underlying iron crust. The absence of fossil remains, especially those typical of open marine conditions such as ammonoids and planktic foraminifera and type B coated grains, that occur in the ferruginous oolithic limestones, suggests that the Villas section was located inland, compared with the RGCH, CHO and PC1 sections where the breccia was not developed and marine remains are dominant.

In the equivalent lithofacies of the AF section (Iberian Range), the same type A and type B iron-coated grains are differentiated as those observed in the ferruginous oolithic limestones from the Prebetic. The mineralogy of these iron-coated grains is mainly composed of goethite, together with calcite, siderite, hematite, kaolinite and illite [19,88]. This mineralogy is quite similar to the reported in this study for the type A iron-coated grains. The electron microscopy images showed that the texture of the type B iron-coated grains from the AF section is similar to that of type B iron-coated grains reported by Reolid et al. [32] in the RGCH section. The environmental conditions for the genesis of the ferruginous oolithic limestone of the AF section are the same as in the Prebetic (PC, CHO, RGCH sections).

5.3. Palaeoclimatic Inferences from Clay Minerals and Geochemical Proxies

Reolid and Abad [21] and Reolid et al. [32] interpreted the iron crust containing iron-coated grains from the PC2 and RGCH sections as plinthitic palaeosols. These authors reported Al-substitution in goethite of 5 mol% in the iron-coated grains and of 10 mol% in the iron crusts, which are quite similar to those obtained for the Villas section (iron crust = 13 mol% and iron-coated grains = 7 mol%), these values being indicators of pedogenic conditions according to the values given by Fitzpatrick and Schwertmann [53].

The mineralogical assemblage reported for the iron crust from the PC2 section [21], is mainly formed by hematite, goethite, kaolinite, illite, calcite, and quartz. By contrast, the crust from the RGCH section does not contain clay minerals, and it is mainly formed by goethite and hematite, together with boehmite and apatite [32]. These differences in the mineralogical content of the iron crusts maybe related to a more or less evolved stage of the plinthitic palaeosols [21]. The iron crust from the PC2 section, which includes poorly developed iron-coated grains with incipient laminations and partial ferruginization, would correspond to a less evolved plinthite, whereas the iron crust from the RGCH section would correspond to a more evolved plinthite [21].

Plinthosols are well-drained lateritic soils with high Fe and/or Al content in relation to other components [89,90]. The term "plinthosol" is defined as an iron-rich mixture of clay minerals (mainly kaolinite) and silica, according to the Food and Agriculture Organization (FAO). This term is equivalent to that of ferrallitic soils categorized by Duchaufour [91] and to the oxisols described by the USDA classification [92].

According to the Fe_2O_3-Al_2O_3-SiO_2 diagram (Figure 7a), the iron crust from the RGCH and PC2 sections plot on the ferrite field due to their high Fe content, whereas the iron crust from the Villas section plots on the kaolinite field but close to that of laterite due to its higher Si and Al content. Therefore, the iron crust from the Villas section may correspond to a less drained plinthosol.

Plinthites develop in tropical environments where elevated temperatures and alternating wet and dry conditions favor the precipitation, mobilization, and accretion of weathered iron oxides [89]. The main process that consumes silicate minerals during chemical weathering is hydrolysis [62]:

$$\text{Hydrolysis} = \text{Al}/\text{Ca} + \text{Mg} + \text{K} + \text{Na} \tag{6}$$

Applying this equation to the studied crusts, it can be determined that the hydrolysis was higher in the iron crust from the Villas section (3.76) than in the iron crust from the PC2 (2.10) and RGCH (0.92) sections. These differences in the hydrolysis intensity can also be inferred from the Fe_2O_3 + MgO-CaO + Na_2O + MgO-Al_2O_3 diagram (Figure 7b), where the low CaO + Na_2O + MgO contents indicate that these elements were weathered and that the Al_2O_3 content is higher in the Villas section due to the immobility of Al during intense chemical weathering.

Sr is more soluble than Ba and Rb during chemical weathering, so higher Ba/Sr and Rb/Sr ratios reflect more weathered rocks [62]. The Ba/Sr and the Rb/Sr are higher in the iron crust from the Villas section (3.58 and 1.10, respectively) than in the iron crust from the RGCH section (0.61 and 0.12, respectively), indicating that the chemical weathering was somewhat more intense in the Villas section (Table 3), which also correlates with the trend observed from watered/disintegrated material (RGCH) to residual soil (Villas) in the Al_2O_3-CaO + Na_2O-K_2O diagram (Figure 7c). The higher fractionation of the REE in the Villas section compared to the RGCH also points to a higher chemical weathering intensity [93].

In soil systems, metal oxides can be scavenged by hematite and goethite [94,95] or being also adsorbed on clay minerals [93], which would explain the different distribution of Ba, Ti, Co, Cr, and Mn in the Fe-rich or kaolinite-rich layers of the iron-coated grains from the Villas section.

The CIA and CIW values lower than 65 reflect compositions of illite, smectite, and feldspar relating to a low degree of chemical weathering, whereas the genesis of kaolinite though intense chemical weathering results in CIA and CIW values close to 100 [66,96–98]. The plinthites studied here show high CIA (from 90.87 to 95.87) and CIW (from 88.14 to 95.59), with the lowest values corresponding to PC2 section (Tables 1 and 3). Sr/Cu ratios higher than 10 indicate hot and dry climates, Sr/Cu ratios between 5 and 10 reflect semi-arid and semi-humid conditions, while Sr/Cu ratios lower than 5 point to a warm and humid climate [99]. Ga/Rb ratios lower than 0.25 agree with cold and dry environments, whereas Ga/Rb ratios higher than 0.25 indicate warm and humid conditions [100]. In the Villas and RGCH sections, both the crusts and the iron-coated grains show Sr/Cu ratios lower than 5 and Ga/Rb higher than 0.25, reflecting warm and humid climatic conditions (Tables 2 and 3).

The higher chemical weathering and palaeoprecipitation regime affecting the Villas sections indicates that the palaeoclimatic conditions were somewhat humid inland in the studied area.

Table 3. CIA, CIW, Ba/Sr, Rb/Sr, Sr/Cu, and Ga/Rb values obtained for the iron crusts from the Villas, RGCH, and PC2 sections and their paleoclimatic significance [66,96,98–100].

CIA			CIW			Ba/Sr		Rb/Sr		Sr/Cu		Ga/Rb	
Villas	RGCH	PC2	Villas	RGCH	PC2	Villas	RGCH	Villas	RGCH	Villas	RGCH	Villas	RGCH
95.20	95.87	90.87	91.99	95.59	88.14	3.58	0.61	1.10	0.12	0.61	0.81	1.52	1.45
CIA or CIW value → Weathering intensity						Higher Ba/Sr and Rb/Sr ratios = Greater weathering				<5	Warm/humid	<0.25	Cold/dry
	<65		Low-moderate							5–10	Semi-arid/ Semi-humid	>0.25	Warm/humid
	>75		High							>10	Hot/dry		

Plate tectonic reconstructions suggest that during the Middle to Upper Jurassic, Iberia was situated at tropical to subtropical latitudes as part of the African plate [101]. This would have provided the necessary palaeoclimatic and paleoenvironmental conditions for the development of the plinthites in the South Iberian Palaeomargin.

With respect to the global palaeoclimatic context, a short warming episode was recorded worldwide in the Middle Callovian [102–105]. However, the end of the Callovian to early Oxfordian was a time of climatic cooling [106,107] as well as a sea-level fall [108]. Many carbonate platforms were exposed, and stratigraphic successions are characterized by the presence of hardgrounds, palaeokarst, and hiatuses [26,109,110].

Similar palaeoclimatic conditions are described in west Iberia. Azerêdo et al. [109] describe a sea-level fall and a change from humid to seasonal semi-arid climatic conditions in the Lusitanian Basin (west-central Portugal) during the Middle–Late Jurassic. According to these authors, a palaeokarstic surface is recorded over the Middle Jurassic carbonates, followed by ferruginous clays (composed of kaolinite and iron oxides) and crust/pisoids, which are consistent with subaerial exposure, as occurs with the plinthitic palaeosols reported in this study.

During the Middle Oxfordian, the decline in $\delta^{18}O$ values is related to rising sea water temperatures [111], accompanied by a secular sea-level rise [106]. In many Tethyan palaeomargins, including the Iberian Palaeomargins, this sea-level rise is recorded as a flooding of the Middle Jurassic carbonate platforms with the recovery of sedimentation and the development of hemipelagic facies [112–114].

The data reported in this study reflect a tropical to subtropical climate during the development of the iron crusts and iron-coated grains at any moment during the Middle Callovian–Early Oxfordian transition in the South Iberian Palaeomargin.

Marine iron ooids with similar textural features as those studied here (type B iron-coated grains) have also been described in Callovian–Oxfordian sections of nearby basins of the Western Tethys (e.g., Paris Basin) [115]. Previous studies indicate that the iron-coated grains in the ferruginous oolithic limestones from the correlatable AF section (Iberian Range, NE Iberia) are a marine rework of iron-coated grains from continental laterites [29,88]. This is congruent with our observations. Therefore, the tropical to subtropical palaeoclimatic conditions occurring during the Middle–Upper Jurassic transition in the South Iberian Palaeomargin may also have taken place in the East Iberian Palaeomargin.

6. Conclusions

The combination of XRD, geochemical, and optical and electron microscopy analysis has allowed the mineralogical and textural characterization of the iron crusts and iron-coated grains from the Central and Eastern External Prebetic (SE Iberia) and the Iberian Range (NE Iberia), drawing the following conclusions:

1. The mineralogical composition of the iron crust is mainly composed of clay minerals (kaolinite, illitic phases, and Ilt/Sme) and/or iron oxides (hematite and goethite), along with the presence of iron-coated grains, this indicates that they are plinthitic palaeosols, characteristic of tropical environments.

2. The platy morphologies of the kaolinite crystals and the presence of book-type aggregates in the matrix of the iron crusts point to an authigenic origin for the kaolinite through chemical weathering processes during the palaeosols development. The kaolinite crystals growing on subhedral illitic phases plates indicate that the illitic phases are previous phases, probably detrital.

3. The mineralogy and texture of the iron-coated grains included in the iron crusts (type A) reflect an in situ origin during the plinthites formation. Subsequent reworking processes caused the break of some of these iron-coated grains that eventually acted as a nucleus of new iron-coated grains. The reworking processes also led to the incorporation of these iron-coated grains into the above ferruginous oolithic limestones (RGCH, CHO, PC, and AF sections) and the ferruginous–carbonated breccia (Villas section). New iron-coated grains (type B) were later formed in the ferruginous oolithic limestones in a marine context.

4. The CIA and CIW values and the Ba/Sr, Rb/Sr, Sr/Cu, and Ga/Rb ratios agree with an intense chemical weathering related to warm and humid conditions during the development of the palaeosols. The higher Ba/Sr ratio value of the iron crust from

the Villas section comparted to that of the RGCH section reflects a higher chemical weathering intensity in the former.

5. The similarity of the iron-coated grains from the equivalent ferruginous oolithic ironstone of the AF section in the Iberian Range suggests the same origin as those from the Central and Eastern External Prebetic. Therefore, the warm and humid conditions related to a tropical climate recorded in the South Iberian Palaeomargin during the Callovian–Oxfordian could have also taken place in the East Iberian Palaeomargin.

References

1. Chamley, H. *Clay Sedimentology*; Springer: Berlin, Germany, 1989; 623p, ISBN 3-540-50889-9.
2. Velde, B. *Origin and Mineralogy of Clays: Clays and the Environment*; Springer: Berlin, Germany, 1995; 334p, ISBN 978-3-540-58012-6.
3. Mack, G.; Calvin, W.; Curtis, H. Classification of paleosols. *Geol. Soc. Am. Bull.* **1993**, *105*, 129–136. [CrossRef]
4. Thiry, M. Palaeoclimatic interpretation of clay minerals in marine deposits: An outlook from the continental origin. *Earth-Sci. Rev.* **2000**, *49*, 201–221. [CrossRef]
5. Tabor, N.J.; Myers, T.S.; Michel, L.A. Sedimentologist's Guide for Recognition, Description, and Classification of Paleosols. In *Terrestrial Depositional Systems: Deciphering Complexities through Multiple Stratigraphic Methods*; Zeigler, K.E., Parker, W.G., Eds.; Elsevier: Amsterdam, The Netherlands, 2017; pp. 165–208, ISBN 9780128032435.
6. Laita, E.; Bauluz, B.; Aurell, M.; Bádenas, B.; Yuste, A. Weathering events recorded in uppermost Hauterivian–lower Barremian clay-dominated continental successions from the NW Iberian Range: Climatic vs. tectonic controls. *J. Iber. Geol.* **2022**, *48*, 45–63. [CrossRef]
7. Raucsik, B.; Varga, A. Climato-environmental controls on clay mineralogy of the Hettangian–Bajocian successions of the Mecsek Mountains, Hungary: An evidence for extreme continental weathering during the early Toarcian oceanic anoxic event. *Palaeogeogr. Palaeoclim. Palaeoecol.* **2008**, *265*, 1–13. [CrossRef]
8. Bauluz, B.; Yuste, A.; Mayayo, M.J.; Canudo, J.I. Early kaolinization of detrital Weald facies in the Galve Sub-basin (Central Iberian Chain, north-east Spain) and its relationship to palaeoclimate. *Cretac. Res.* **2014**, *50*, 214–227. [CrossRef]
9. Laita, E.; Bauluz, B.; Aurell, M.; Bádenas, B.; Canudo, J.I.; Yuste, A. A change from warm/humid to cold/dry climate conditions recorded in lower Barremian clay-dominated continental successions from the SE Iberian Chain (NE Spain). *Sediment. Geol.* **2020**, *403*, 105673. [CrossRef]
10. Righi, D.; Meunier, A. Origin of Clays by Rick Weathering and Soil Formation. In *Origin and Mineralogy of Clays. Clays and the Environment*; Velde, B., Ed.; Springer: Berlin/Heidelberg, Germany; New York, NY, USA, 1995; pp. 43–161, ISBN 978-3-540-75633-0.
11. Campo, M.D.; Bauluz, B.; del Papa, C.; White, T.; Yuste, A.; Mayayo, M.J. Evidence of cyclic climatic changes recorded in clay mineral assemblages from a continental Paleocene-Eocene sequence, northwestern Argentina. *Sediment. Geol.* **2018**, *368*, 44–57. [CrossRef]
12. Wilson, M.J. The origin and formation of clay minerals in soils: Past, present and future perspectives. *Clay Miner.* **1999**, *34*, 7–25. [CrossRef]
13. Galán, E. Genesis of clay minerals. In *Developments in Clay Science*; Bergaya, F., Theng, B.K.G., Lagaly, G., Eds.; Elsevier: Amsterdam, The Netherlands, 2006; pp. 1129–1162.

14. Dera, G.; Pellenard, P.; Neige, P.; Deconinck, J.-F.; Pucéat, E.; Dommergues, J.-L. Distribution of clay minerals in Early Jurassic Peritethyan seas: Palaeoclimatic significance inferred from multiproxy comparisons. *Palaeogeogr. Palaeoclim. Palaeoecol.* **2009**, *271*, 39–51. [CrossRef]

15. Cecca, F.; Garin, B.M.; Marchand, D.; Lathuiliere, B.; Bartolini, A. Paleoclimatic control of biogeographic and sedimentary events in Tethyan and peri-Tethyan areas during the Oxfordian (Late Jurassic). *Palaeogeogr. Palaeoclim. Palaeoecol.* **2005**, *222*, 10–32. [CrossRef]

16. Bucur, I.I.; Reolid, M. Incidence of the early Toarcian global change on Dasycladales (Chlorophyta) and the subsequent recovery: Comparison with end-Triassic Mass Extinction. *Earth-Sci. Rev.* **2024**, *249*, 104666. [CrossRef]

17. Aurell, M.; Bádenas, B.; Bello, J.; Delvene, G.; Meléndez, G.; Pérez-Urresti, I.; Ramajo, J. El Calloviense y el Jurásico Superior en la Cordillera Ibérica Nororiental y la zona de enlace con la Cordillera Costero Catalana, en los sectores de Sierra de Arcos, Calanda y Xerta-Paüls. *Cuad. Geol. Ibér.* **1999**, *25*, 73–110.

18. Kadiri, K. Jurassic ferruginous hardgrounds of the "Dorsale Calcaire" and the Jbel Moussa Group (Internal Rif, Morocco): Stratigraphical context and paleoceanographic consequences of mineralization processes. *Geol. Romana* **2002**, *36*, 33–69.

19. Ramajo, J.; Aurell, M.; Cepría, J. Análisis de facies de la Capa de oolitos ferruginosos de Arroyofrío en la Sierra de Arcos (Jurásico, Cordillera Ibérica septentrional). *J. Iber. Geol.* **2002**, *28*, 45–64.

20. Reolid, M.; El Kadiri, K.; Abad, I.; Olóriz, F.; Jiménez-Millán, J. Jurassic microbial communities in hydrothermal manganese crust of the Rifian Calcareous Chain, Northern Morocco. *Sediment. Geol.* **2011**, *233*, 159–172. [CrossRef]

21. Reolid, M.; Abad, I. The Middle-Upper Jurassic unconformity in the South Iberian Palaeomargin (Western Tethys): A history of carbonate platform fragmentation, emersion and subsequent drowning. *J. Iber. Geol.* **2019**, *45*, 87–110. [CrossRef]

22. Picard, S.; Garcia, J.P.; Le'cuyer, C.; Sheppard, S.; Capetta, H.; Emig, C. δ18O values of co- existing brachiopods and fish temperature di¡erences and estimates of paleodepths. *Geology* **1998**, *26*, 975–978. [CrossRef]

23. Podlaha, O.G.; Mutterlose, J.; Veizer, J. Preservation of δ^{18}O and δ^{13}C in belemnite rostra from the Jurassic/early Cretaceous successions. *Am. J. Sci.* **1998**, *298*, 324–347. [CrossRef]

24. Price, G.D. The evidence and implications of polar ice during the Mesozoic. *Earth-Sci. Rev.* **1999**, *48*, 183–210. [CrossRef]

25. Dromart, G.; Garcia, J.-P.; Picard, S.; Atrops, F.; Lécuyer, C.; Sheppard, S. Ice age at the Middle–Late Jurassic transition? *Earth Planet. Sci. Lett.* **2003**, *213*, 205–220. [CrossRef]

26. Norris, M.S.; Hallam, A. Facies variations across the Middle-Upper Jurassic boundary in Western Europe and the relationship to sea-level changes. *Palaeogeogr. Palaeoclim. Palaeoecol.* **1995**, *116*, 189–245. [CrossRef]

27. Gygi, R.A.; Coe, A.L.; Vail, P.R. Sequence stratigraphy of the Oxfordian and Kimmeridgian stages (Late Jurassic) in northern Switzerland. Mesozoic and Cenozoic Sequence Stratigraphy of European Basins. *SEPM Spec. Publ.* **1998**, *60*, 527–544.

28. Leinfelder, R.R.; Wilson, R.C. Third-Order Sequences in an Upper Jurassic Rift-Related Second-Order Sequence, Central Lusitanian Basin, Portugal. Mesozoic and Cenozoic Sequence Stratigraphy of European Basins. *SEPM Spec. Publ.* **1998**, *60*, 507–525.

29. Aurell, M.; Fernandez-Lopez, S.; Melendez, G. The Middle-Upper Jurassic ooliticironstone level in the Iberian range (Spain). Eustatic implications. *Geobios* **1994**, *27*, 549–561. [CrossRef]

30. Courville, P.; Collin, P.Y. La série du Callovien et de l'Oxfordien de Veuxhaulles (Châtillonnais, Côte d'Or): Problèmes de datation, de géométrie et de paléoenvironnements dans une série "condensée". *Bull. Sci. Bourgogne* **1997**, *49*, 29–43.

31. Olóriz, F.; Reolid, M.; Rodríguez-Tovar, F.J. Taphonomy of fossil macro-invertebrate assemblages as a tool for ecostratigraphic interpretation in Upper Jurassic shelf deposits (Prebetic Zone, southern Spain). *Geobios* **2008**, *41*, 31–42. [CrossRef]

32. Reolid, M.; Abad, I.; Martín-García, J.M. Palaeoenvironmental implications of ferruginous deposits related to a Middle–Upper Jurassic discontinuity (Prebetic Zone, Betic Cordillera, Southern Spain). *Sediment. Geol.* **2008**, *203*, 1–16. [CrossRef]

33. García-Hernández, M.; López-Garrido, A.C.; Rivas, P.; Sanz de Galdeano, C.; Vera, J.A. Mesozoic paleogeographic evolution in the external zones of the Betic Cordillera (Spain). *Geol. Mijnbouw.* **1980**, *59*, 155–168.

34. Martín-Algarra, A.; Vera, J.A. La Cordillera Bética y las Baleares en el contexto del 996 Mediterráneo Occidental. In *Geología de España*; Vera, J.A., Ed.; Instituto Geológico y Minero de España: Madrid, Spain, 2004; 884p, ISBN 978-8478405466.

35. Jerez-Mir, L. Geología de la Zona Prebética en la Transversal de Elche de la Sierra y Sectores Adyacentes (Provincias de Albacete y Murcia). Ph.D. Thesis, Universidad de Granada, Granada, Spain, 1973.

36. García-Hernández, M.; López-Garrido, A.C.; Martín-Algarra, A.; Molina, J.M.; Ruiz-Ortiz, P.A.; Vera, J.A. Las discontinuidades mayores del Jurásico de las Zonas Externas de las Cordilleras Béticas: Análisis e interpretación de los ciclos sedimentarios. *Cuad. Geol. Ibérica.* **1989**, *13*, 35–52.

37. Reolid, M.; Molina, J.M.; Nieto, L.M.; Rodríguez-Tovar, F.J. *The Toarcian Oceanic Anoxic Event in the South Iberian Palaeomargin*; Springer Nature: Berlin, Germany, 2018.

38. López-Garrido, A.C.; García-Hernández, M. Ciclos sedimentarios mayores en la primera fase carbonatada de la plataforma prebética (Lías-Valanginiense inferior). *II Congr. Geol. España* **1988**, *SGE 1*, 107–110.

39. Foucault, A. Etude Géologique des Environs des Sources du Guadalquivir (Provinces de Jaen et de Grenade, Espagne Méridionale). Ph.D. Thesis, University of Paris, Paris, France, 1971.

40. Reolid, M. Dinámica Eco-Sedimentaria Durante el Oxfordiense Medio-Kimmeridgiense Temprano en la Zona Prebética: Interpretación Ecoestratigráfica y Secuencial. Ph.D. Thesis, Universidad de Granada, Granada, Spain, 2003.

41. Pendas, F. Definición morfológica de los embalses subterráneos del alto sureste español. *I Congr. Hisp. Luso-Am. Geol. Económica Sección Hidrogeol.* **1971**, *2*, 529–550.

42. Rodríguez-Estrella, T. Geología e Hidrogeología del Sector de Alcaraz-Lietor-Yeste (Prov. de Albacete). Síntesis Geológica de la Zona Prebética. Ph.D. Thesis, Universidad de Granada, Granada, Spain, 1978.

43. Rodríguez-Tovar, F.J. Evolución Sedimentaria y Ecoestratigráfica en Plataformas Epicontinentales del Margen Subibérico Durante el Kimmeridgiense Inferior. Ph.D. Thesis, Universidad de Granada, Granada, Spain, 1993.

44. Olóriz, F.; Reolid, M.; Rodríguez-Tovar, F. Fossil assemblages, lithofacies, taphofacies and interpreting depositional dynamics in the epicontinental Oxfordian of the Prebetic Zone, Betic Cordillera, southern Spain. *Palaeogeogr. Palaeoclim. Palaeoecol.* **2002**, *185*, 53–75. [CrossRef]

45. Olóriz, F.; Reolid, M.; Rodríguez-Tovar, F.J. A Late Jurassic carbonate ramp colonized by sponges and benthic microbial communities (External Prebetic, southern Spain). *Palaios* **2003**, *18*, 528–545. [CrossRef]

46. Gómez, J.J.; Goy, A. Las unidades litoestratigráficas del Jurásico medio y superior, en facies carbonatadas del sector levantino de la Cordillera Ibérica. *Estud. Geol.* **1979**, *35*, 569–598.

47. Linares-Girela, L. Datos sobre las series Jurásico-Cretácicas en el sector de Peñas de S. Pedro-Chinchilla de Montearagón (prov. de Albacete). *Bol. Geol. Min.* **1976**, *XXXVII-IV*, 355–364.

48. Martin-Islán, J.D. Using XPowder: A Software Package for Powder X-ray Diffraction Analysis. Available online: www.xpowder.com (accessed on 25 June 2024).

49. Biscaye, P.E. Mineralogy and sedimentation of recent deep-sea clay in the Atlantic Ocean and adjacent seas and oceans. *Geol. Soc. Am. Bull.* **1965**, *76*, 803–832. [CrossRef]

50. Schultz, L.G. *Quantitative Interpretation of Mineralogical Composition From X-ray and Chemical Data for the Pierre Shale*; USGS Professional Paper 391-C; U.S. Government Publishing Office: Washington, DC, USA, 1964; pp. 1–30.

51. Smith, D.K.; Johnson, G.G., Jr. Digitized database quantification, DDBQ, analysis of complex mixtures using fully digitized patterns. *Adv. X-ray Anal.* **2000**, *42*, 276–286.

52. Hillier, S. Quantitative analysis of clay and other minerals in sandstones by X-ray powder diffraction (XRPD). In *Clay Mineral Cements in Sandstones*; Worden, R.H., Morad, E., Eds.; Blackwell Publishing: Malden, MA, USA, 2003; pp. 213–251, ISBN 1-40510-587-9.

53. Fitzpatrick, R.; Schwertmann, U. Al-substituted goethite—An indicator of pedogenic and other weathering environments in South Africa. *Geoderma* **1982**, *27*, 335–347. [CrossRef]

54. Schulze, D.G. The Influence of Aluminum on Iron Oxides. VIII. Unit-Cell Dimensions of Al-Substituted Goethites and Estimation of Al from them. *Clays Clay Miner.* **1984**, *32*, 36–44. [CrossRef]

55. Bárdossy, G. Karst Bauxites. In *Developments in Economic Geology*; Elsevier: Amsterdam, The Netherlands, 1982; 441p.

56. Whitney, D.L.; Evans, B.W. Abbreviations for names of rock-forming minerals. *Am. Mineral.* **2010**, *95*, 185–187. [CrossRef]

57. Nesbitt, H.W.; Young, G.M. Early Proterozoic climates and plate motions inferred from major element chemistry of lutites. *Nature* **1982**, *299*, 715–717. [CrossRef]

58. Harnois, L. The CIW index: A new chemical index of weathering. *Sediment. Geol.* **1988**, *55*, 319–322. [CrossRef]

59. Sheldon, N.D.; Retallack, G.J.; Tanaka, S. Geochemical Climofunctions from North American Soils and Application to Paleosols across the Eocene-Oligocene Boundary in Oregon. *J. Geol.* **2002**, *110*, 687–696. [CrossRef]

60. Guerrak, S. Metallogenesis of cratonic oolitic ironstone deposits in the Bled el Mass, Azzel Matti, Ahnet and Mouydir basins, Central Sahara, Algeria. *Int. J. Earth Sci.* **1987**, *76*, 903–922. [CrossRef]

61. Aleva, G.J.J. *Laterites: Concepts, Geology, Morphology and Chemistry*; International Soil Reference and Information Centre (ISRIC): Wageningen, The Netherlands, 1994; 169p, ISBN 90.6672.053.0.

62. Mitchell, R.L.; Sheldon, N.D. Sedimentary provenance and weathering processes in the 1.1 Ga Midcontinental Rift of the Keweenaw Peninsula, Michigan, USA. *Precambrian Res.* **2016**, *275*, 225–240. [CrossRef]

63. Nesbitt, H.; Young, G. Prediction of some weathering trends of plutonic and volcanic rocks based on thermodynamic and kinetic considerations. *Geochim. Cosmochim. Acta* **1984**, *48*, 1523–1534. [CrossRef]

64. Taylor, S.R.; McLennan, S.M. *The Continental Crust: Its Composition and Evolution*; Blackwell: Oxford, UK, 1985; ISBN 0632011483.

65. Yuste, A.; Camacho, I.; Bauluz, B.; Mayayo, M.J.; Laita, E. Palaeoweathering events recorded on siliciclastic continental deposits (Albian, Lower Cretaceous) in NE Spain. *Appl. Clay Sci.* **2020**, *190*, 105598. [CrossRef]

66. Bauluz, B.; Mayayo, M.J.; Fernandez-Nieto, C.; Lopez, J.M.G. Geochemistry of Precambrian and Paleozoic siliciclastic rocks from the Iberian Range NE Spain: Implications for source-area weathering, sorting, provenance, and tectonic setting. *Chem. Geol.* **2000**, *168*, 135–150. [CrossRef]

67. Lanson, B.; Beaufort, D.; Berger, G.; Bauer, A.; Cassagnabère, A.; Meunier, A. Authigenic kaolin and illitic minerals during burial diagenesis of sandstones: A review. *Clay Miner.* **2002**, *37*, 1–22. [CrossRef]

68. Brosse, E.; Margueron, T.; Cassou, C.; Sanjuan, B.; Canham, A.; Girad, J.P.; Lacharpahne, J.C.; Sommer, F. The formation and stability of kaolinite in Brent sandstone reservoirs: A modelling approach. In *Clay Mineral Cements in Sandstones*; Worden, R.H., Morad, S., Eds.; Blackwell Publishing: Malden, MA, USA, 2003; pp. 383–408, ISBN 1-40510-587-9.

69. Jeong, G.Y.; Hillier, S.; Kemp, R.A. Changes in mineralogy of loess–paleosol sections across the Chinese Loess Plateau. *Quat. Res.* **2011**, *75*, 245–255. [CrossRef]

70. Schaetzl, R.; Thompson, M.L. *Soils: Genesis and Geomorphology*; Cambridge University Press: Cambridge, UK, 2015; 779p, ISBN 978-1-107-01693-4.

71. Meenakshi; Shrivastava, J.; Chandra, R. Pedogenically degenerated illite and chlorite lattices aid to palaeoclimatic reconstruction for chronologically constrained (8–130 ka) loess-palaeosols of Dilpur Formation, Kashmir, India. *Geosci. Front.* **2020**, *11*, 1353–1367. [CrossRef]

72. Entrena, A.; Fornós, J.J.; Auqué, L.F.; Gràcia, F.; Laita, E. Mineralogical and Sedimentological Characterization of the Clay-Rich Sediments from Ases Cave (Cova Dets Ases, Mallorca, Spain): Origin and Classification. *Minerals* **2022**, *12*, 1473. [CrossRef]

73. Youssef, E.S.A. Sedimentological studies on the central Wadi Kalabsha kaolin deposits, Southwest of Aswan, Egypt. *J. Miner. Pet. Econ. Geol.* **1996**, *91*, 353–363. [CrossRef]

74. Kenny, R.; Krinsley, D.H. Silicified Mississippian Paleosol Microstructures: Evidence for Ancient Microbial-Soil Associations. *Scanning Microsc.* **1992**, *6*, 359–366.

75. Mahaney, W.; Krinsley, D.; Allen, C.; Ditto, J.; Langworthy, K.; Batchelor, A.; Lecompte, M.; Milner, M.; Hart, K.; O'Reilly, S.S.; et al. Reassessment of the Microbial Role in Mn-Fe Nodule Genesis in Andean Paleosols. *Geomicrobiol. J.* **2015**, *32*, 27–41. [CrossRef]

76. Szamatek, K.; Barczuk, A.; Youssed, E.A.A. Genesis and mineralogy of lateritic kaolin at Aswan area (Sw Egypt). *Arch. Mineral. (Wars.)* **1993**, *2*, 81–97.

77. Taylor, G.; Eggleton, R.A.; Foster, L.D.; Tilley, D.B.; Le Gleuher, M.; Morgan, C.M. Nature of the Weipa Bauxite deposit, northern Australia. *Aust. J. Earth Sci.* **2008**, *55*, S45–S70. [CrossRef]

78. Retallack, G.J. *Soils of the Past*; Blackwell Science: Malden, MA, USA, 2001; 30p.

79. Bhattacharyya, D.P.; Kakimoto, P.K. Origin of ferriferous ooids: An SEM study of ironstone ooids and bauxite pisoids. *J. Sediment. Petrol.* **1982**, *53*, 849–857.

80. Mücke, A.; Badejoko, T.A.; Akande, S.O. Petrographic-microchemical studies and origin of the Agbaja Phanerozoic Ironstone Formation, Nupe Basin, Nigeria: A product of a ferruginized ooidal kaolin precursor not identical to the Minette-type. *Miner. Depos.* **1999**, *34*, 284–296. [CrossRef]

81. Aurell, M.; Bádenas, B.; Castanera, D.; Gasca, J.; Canudo, J.; Laita, E.; Liesa, C. Latest Jurassic–Early Cretaceous synrift evolution of the Torrelapaja Subbasin (Cameros Basin): Implications for Northeast Iberia palaeogeography. *Cretac. Res.* **2021**, *128*, 104997. [CrossRef]

82. Marques, B.; Olóriz, F.; Rodríguez-Tovar, F.J. Interactions between tectonics and eustasy during the Upper Jurassic and lowermost Cretaceous. Examples from the south ofIberia. *Bull. Soc. Géol. Fr.* **1991**, *162*, 1109–1124.

83. Aurell, M.; Robles, S.; Bádenas, B.; Rosales, I.; Quesada, S.; Meléndez, G.; García-Ramos, J. Transgressive–regressive cycles and Jurassic palaeogeography of northeast Iberia. *Sediment. Geol.* **2003**, *162*, 239–271. [CrossRef]

84. Legarreta, L. Evolution of a Callovian-Oxfordian carbonate margin in the Neuquén Basin of west-central Argentina: Facies, architecture, depositional sequences and global sea-level changes. *Sediment. Geol.* **1991**, *70*, 209–240. [CrossRef]

85. Hallam, A. A review of the broad pattern of Jurassic sea-level changes and their possible causes in the light of current knowledge. *Palaeogeogr. Palaeoclim. Palaeoecol.* **2001**, *167*, 23–37. [CrossRef]

86. Olóriz, F.; Reolid, M.; Rodríguez-Tovar, F.J. Taphonomy of fossil macroinvertebrates for improving ecostratigraphy: Shifting eco-sedimentary conditions from carbonate to carbonate-siliciclastic shelf (Upper Jurassic, Prebetic Zone). *Geobios* **2005**, *2*, 123–124.

87. Lechte, M.; Halverson, G.; Wallace, M.; Gibson, T.; van Smeerdijk Hood, A.; Wang, C.; Bui, T.H.; Maloney, K.; Millikin, A. Oolitic ironstones, continental iron flux and reverse weathering in the Proterozoic Eon: Insights from the Tonian Katherine Group, Yukon. *Earth-Sci. Rev.* **2024**, *253*. [CrossRef]

88. Aurell, M. El Jurásico Superior de la Cordillera Ibérica Central (Provincias de Zaragoza y Teruel). Análisis de Cuenca. Ph.D. Thesis, Universidad de Zaragoza, Zaragoza, Spain, 1990.

89. Eze, P.; Udeigwe, T.; Meadows, M. Plinthite and Its Associated Evolutionary Forms in Soils and Landscapes: A Review. *Pedosphere* **2014**, *24*, 153–166. [CrossRef]

90. Luko-Sulato, K.; Mounier, S.; Furlan, L.M.; Govone, J.S.; Bueno, G.T.; Rosolen, V. Spatial variation of soil organic matter and metal mobility in wetland soils: Implications for biogeochemical processes in lateritic landscape. *Catena* **2024**, *237*. [CrossRef]

91. Duchaufour, P. *Pedology. Pedogénesis and Classification*; Springer: New York, NY, USA, 1982; 462p, ISBN 978-9401160056.

92. Fookes, P.G. A Review: Genesis and classification of tropical residual soils for engineers. In *Geotechnics in the African Environment*; Blight, G.E., Fourie, A.B., Luker, I., Mouton, D.J., Scheurenberg, R.J., Eds.; CRC Press: Rotterdam, The Netherlands, 1994; pp. 423–442, ISBN 978-90-5410-007-2.

93. Laita, E.; Bauluz, B.; Yuste, A. The role of clay minerals in the concentration and distribution of critical metals in lateritic palaeosols from NE Iberia. *Appl. Clay Sci.* **2024**, *249*, 107264. [CrossRef]

94. McLaren, R.G.; Lawson, D.M.; Swift, R.S. Sorption and desorption of cobalt by soils and soil components. *Eur. J. Soil Sci.* **1986**, *37*, 413–426. [CrossRef]

95. Bradl, H.B. Adsorption of heavy metal ions on soils and soils constituents. *J. Colloid Interface Sci.* **2004**, *277*, 1–18. [CrossRef] [PubMed]

96. Price, J.R.; Velbel, M.A. Chemical weathering indices applied to weathering profiles developed on heterogeneous felsic metamorphic parent rocks. *Chem. Geol.* **2003**, *202*, 397–416. [CrossRef]

97. Bahlburg, H.; Dobrzinski, N. A Review of the Chemical Index of Alteration (CIA) and Its Application to the Study of Neoproterozoic Glacial Deposits and Climate Transitions. In *The Geological Record of Neoproterozoic Glaciations*; Memoir 36; Arnaud, E., Halverson, G.P., ShieldsZhou, G.A., Eds.; Geological Society: London, UK, 2011; pp. 81–92.

98.   Fathy, D.; Abart, R.; Wagreich, M.; Gier, S.; Ahmed, M.S.; Sami, M. Late Campanian Climatic-Continental Weathering Assessment and Its Influence on Source Rocks Deposition in Southern Tethys, Egypt. *Minerals* **2023**, *13*, 160. [CrossRef]

99.   Lerman, A.; Imboden, D.M.; Gat, J.R. *Physics and Chemistry of Lakes*; Springer: Berlin, Germany, 1995; 334p, ISBN 978-3-642-85134-6.

100.   Xu, J.; Liu, Z.; Bechtel, A.; Meng, Q.; Sun, P.; Jia, J.; Cheng, L.; Song, Y. Basin evolution and oil shale deposition during Upper Cretaceous in the Songliao Basin (NE China): Implications from sequence stratigraphy and geochemistry. *Int. J. Coal Geol.* **2015**, *149*, 9–23. [CrossRef]

101.   Stampfli, G.; Borel, G. A plate tectonic model for the Paleozoic and Mesozoic constrained by dynamic plate boundaries and restored synthetic oceanic isochrons. *Earth Planet. Sci. Lett.* **2002**, *196*, 17–33. [CrossRef]

102.   Dromart, G.; Garcia, J.-P.; Gaumet, F.; Picard, S.; Rousseau, M.; Atrops, F.; Lecuyer, C.; Sheppard, S.M.F. Perturbation of the carbon cycle at the Middle/Late Jurassic transition: Geological and geochemical evidence. *Am. J. Sci.* **2003**, *303*, 667–707. [CrossRef]

103.   Pellenard, P.; Fortwengler, D.; Marchand, D.; Thierry, J.; Bartolini, A.; Boulila, S.; Pierre-Yves Collin, P.-Y.; Enay, R.; Galbrun, B.; Gardin, S.; et al. Integrated stratigraphy of the Oxfordian global stratotype section and point (GSSP) candidate in the Subalpine Basin (SE France). *Vol. Jurass.* **2014**, *12*, 1–44.

104.   Carmeille, M.; Bourillot, R.; Pellenard, P.; Dupias, V.; Schnyder, J.; Riquier, L.; Mathieu, O.; Brunet, M.-F.; Enay, R.; Grossi, V.; et al. Formation of microbial organic carbonates during the Late Jurassic from the Northern Tethys (Amu Darya Basin, Uzbekistan): Implications for Jurassic anoxic events. *Glob. Planet. Chang.* **2020**, *186*, 103127. [CrossRef]

105.   Price, G.D.; Heszler, B.; Charlton, L.-M.T.; Cox, J. A climate perturbation at the Middle–Late Jurassic Transition? Evaluating the isotopic evidence from south-central England. *Palaeogeogr. Palaeoclim. Palaeoecol.* **2023**, *628*, 111755. [CrossRef]

106.   Lécuyer, C.; Picard, S.; Garcia, J.; Sheppard, S.M.F.; Grandjean, P.; Dromart, G. Thermal evolution of Tethyan surface waters during the Middle-Late Jurassic: Evidence from δ^{18}O values of marine fish teeth. *Paleoceanography* **2003**, *18*. [CrossRef]

107.   Wierzbowski, H. Seawater temperatures and carbon isotope variations in central European basins at the Middle–Late Jurassic transition (Late Callovian–Early Kimmeridgian). *Palaeogeogr. Palaeoclim. Palaeoecol.* **2015**, *440*, 506–523. [CrossRef]

108.   Haq, B.U. Jurassic sea-level variations: A reappraisal. *GSA Today* **2018**, *28*, 4–10. [CrossRef]

109.   Azerêdo, A.C.; Wright, V.P.; Ramalho, M.M. The Middle–Late Jurassic forced regression and disconformity in central Portugal: Eustatic, tectonic and climatic effects on a carbonate ramp system. *Sedimentology* **2002**, *49*, 1339–1370. [CrossRef]

110.   Lorin, S.; Courville, P.; Collin, P.Y.; Thierry, J.; Tort, A. Modalités de réinstallation d'une plate-forme carbonatée après une crise sédimentaire: Exemple de la limite Oxfordien moyen—Oxfordien supérieur dans le Sud-Est du Bassin de Paris. *Bull. Soc. Géol. Fr.* **2004**, *175*, 289–302. [CrossRef]

111.   Dera, G.; Brigaud, B.; Monna, F.; Laffont, R.; Pucéat, E.; Deconinck, J.-F.; Pellenard, P.; Joachimski, M.M.; Durlet, C. Climatic ups and downs in a disturbed Jurassic world. *Geology* **2011**, *39*, 215–218. [CrossRef]

112.   Martire, L. Stratigraphy, facies and synsedimentary tectonics in the Jurassic Rosso Ammonitico Veronese (Altopiano di Asiago, NE Italy). *Facies* **1996**, *35*, 209–236. [CrossRef]

113.   Olóriz, F.; Marques, B.; Caracuel, J.E. The Middle-Upper Oxfordian of Central Sierra Norte (Mallorca, Spain), and progressing ecostratigraphic approach in Western Tethys. *Geobios* **1998**, *31*, 319–336. [CrossRef]

114.   Coimbra, R.; Immenhauser, A.; Olóriz, F.; Rodríguez-Galiano, V.; Chica-Olmo, M. New insights into geochemical behaviour in ancient marine carbonates (Upper Jurassic Ammonitico Rosso): Novel proxies for interpreting sea-level dynamics and palaeoceanography. *Sedimentology* **2015**, *62*, 266–302. [CrossRef]

115.   Collin, P.Y.; Loreau, J.P.; Courville, P. Depositional environments and iron ooid formation in condensed sections (Callovian–Oxfordian, south-eastern Paris basin, France). *Sedimentology* **2005**, *52*, 969–985. [CrossRef]